Piezo1 mechanosensing regulates integrin-dependent chemotactic migration in human T cells

Chinky Shiu Chen Liu[1], Tithi Mandal[2], Parijat Biswas[3], Md. Asmaul Hoque[1,4], Purbita Bandopadhyay[1,4], Bishnu Prasad Sinha[1,4], Jafar Sarif[1,4], Ranit D'Rozario[1,4], Deepak Kumar Sinha[3], Bidisha Sinha[2], Dipyaman Ganguly[1]*

[1]IICB-Translational Research Unit of Excellence, CSIR-Indian Institute of Chemical Biology, Kolkata, India.

[2]Department of Biological Sciences, Indian Institute of Science Education and Research, Kolkata, India.

[3] Department of Biological Sciences, Indian Association for Cultivation of Science, Kolkata, India.

[4]Academy of Scientific and Innovative Research, Ghaziabad, India.

Correspondence: dipyaman@iicb.res.in

Running title: Piezo1 mechanosensing in human T cell chemotaxis

Keywords: Human T cells, Piezo1, Mechanosensing, Migration, Chemokine, Chemotaxis, Focal adhesion kinase, LFA-1, F-actin, Confocal Microscopy, Interference Reflection Microscopy

ABSTRACT

T cells are crucial for efficient antigen-specific immune responses and thus their migration within the body, to inflamed tissues from circulating blood or to secondary lymphoid organs, play a very critical role. T cell extravasation in inflamed tissues depends on chemotactic cues and interaction between endothelial adhesion molecules and cellular integrins. A migrating T cell is expected to sense diverse external and membrane-intrinsic mechano-physical cues, but molecular mechanisms of such mechanosensing in cell migration are not established. We explored if the professional mechanosensor Piezo1 play any role during integrin-dependent chemotaxis of human T cells. We found that deficiency of Piezo1 in human T cells interfered with integrin-dependent cellular motility on ICAM-1-coated surface. Piezo1 recruitment at the leading edge of moving T cells is dependent on and follows focal adhesion formation at the leading edge and local increase in membrane tension on chemokine receptor activation. Piezo1 recruitment and activation, followed by calcium influx and calpain activation, in turn are crucial for the integrin LFA-1 (CD11a/CD18) recruitment at the leading edge of the chemotactic human T cells. Thus, we find that Piezo1 activation in response to local mechanical cues constitutes a membrane-intrinsic component of the 'outside-in' signaling in human T cells, migrating in response to chemokines, that mediates integrin recruitment to the leading edge.

INTRODUCTION

Efficient T cell migration from blood circulation to secondary lymphoid organs and inflamed tissue is paramount for optimal tissue antigen sampling and effector functions during adaptive immune response (1-4). The process is dependent on chemotactic cues, interaction between endothelial adhesion molecules and T cell integrins, and an intricate acto-myosin dynamics (5). Generation of mechanical force is critical to propel migrating cells (6-9). Mechanosensing of the substrate and increase in cellular membrane tension is also intuitively apparent in a migrating T cell, although mechanistic details are not explored to a great extent.

Piezo1 and Piezo2 ion channels are evolutionarily conserved professional mechanosensors that can sense increase in membrane tension mostly independent of other protein-protein interactions (10-12). Mechanosensing by Piezo1 has been demonstrated to play critical role in diverse patho-physiologic contexts given its wide tissue expression including the immunocellular compartment (13-21). We previously identified crucial role of this specialized mechanotransducer in optimal TCR triggering (14, 19). The immunocellular expression of Piezo1 thus makes it a strong candidate for mechanosensing at the plasma membrane to regulate motility of immune cells. Piezo1 shows differential involvement in cellular migration depending on context (22- 28). Previous studies point to the possibility of a role of Piezo1 in confinement sensing and integrin activation in moving cells, while it deters integrin-independent cell motility, usually referred to as amoeboid movement (29, 30).

Here we aimed at exploring if Piezo1 mechanosensing plays any role during integrin-dependent chemotactic migration of human T cell migration, a patho-physiologically critical event in an ongoing immune response as well as in the steady-state. We found that deficiency of Piezo1 expression in human $CD4^+$ T cells as well as Jurkat T cells interfered with efficient integrin-dependent cellular motility in response to a chemotactic cue. We also found that Piezo1 activation constitutes a hitherto unknown membrane-intrinsic component of the 'outside-in' signaling in human T cells in response to chemokine receptor activation, that follows activation of focal adhesion kinase leading to local increase in membrane tension and mediates local recruitment of integrin molecules at the leading edge of the moving human T cells.

RESULTS

Piezo1 deficiency abrogates integrin-dependent chemotactic motility in human T cells

65 We first assessed the role of Piezo1 on integrin-dependent, non-directional motility of primary human
66 $CD4^+$ T cells. We used GFP plasmid and Piezo1 siRNA co-transfected cells to facilitate distinction
67 between potentially transfected and untransfected cells during cell tracking. We compared the
68 motility of GFP^+ T cells (presuming they had a good transfection efficiency and thus will also have the
69 siRNA) with the GFP^- T cells in the same culture. This was confirmed by flow cytometric assessment of
70 Piezo1 protein content on the T cell surface as well as the whole T cells (Figure 1-figure supplement
71 1B & C). Piezo1 deficiency in T cells (potentially GFP^+) significantly hindered their migration in response
72 to CCL19 in terms of its mean-squared displacement (MSD, Figure 1A-C). Representative cell tracks of
73 Piezo1 deficient (GFP^+) and control (GFP^-) are shown in Figure 1B, Figure1-figure supplement 1D and
74 Video 1. These results were further confirmed in a separate experiment where Piezo1 knockdown
75 $CD4^+$ T cells showed significant reduction in motility compared to control siRNA-transfected cells
76 (Figure 1-figure supplement 1E).

77 ICAM1-coated transwell chemotaxis assay of human $CD4^+$ T lymphocytes and Jurkat T cells also
78 showed significant reduction in migration upon siRNA-mediated Piezo1 knockdown, in response to
79 CCL19 and SDF1α gradients, respectively (Figure 1D, E). Piezo1 inhibition with GsMTx4 also led to
80 significant impairment of transwell chemotaxis of $CD4^+$ T cells (Figure 1-figure supplement 1F).

81

82 **Redistribution of Piezo1 toward the leading edge of migrating T cells in response to chemotactic cue**

83 Cell polarity is a crucial aspect of directional cell motility in response to chemokines. $CD4^+$ T cells
84 seeded on ICAM-1 bed showed striking polarity in Piezo1 distribution, upon stimulation with CCL19
85 for 15 minutes (Figure 1F, G; Video 2). Piezo1 m-Cherry expressing Jurkat T cells also showed striking
86 leading edge polarity in the presence of SDF1α under ICAM1 adhesion (Figure 1H). In Figure 1I, particle
87 image velocimetry (PIV) analysis of a single representative Jurkat cell has been shown to display the
88 dynamically polarized Piezo1 fluorescence upon SDF1α treatment with time, as opposed to rather
89 uniformly distributed Piezo1 signals in a representative untreated cell. The continuous redistribution
90 of Piezo1 within the motile T cells towards the leading edge can also be appreciated in the
91 representative moving image provided (Video 3). Redistribution of Piezo1 to the leading edge of
92 chemokine-stimulated $CD4^+$ T cells was confirmed from its anti-polar localization to CD44, which
93 preferentially accumulates at the uropod of moving T cells (Figure 1-figure supplement 1G, H)

94

95 **Piezo1 redistribution in migrating T cells follow increased membrane tension in the leading edge**

96 Piezo1 is a professional mechanosensor ion channel, which senses increase in plasma membrane
97 tension and responds by driving calcium influx into the cells (14, 19, 31). As T cells migrate on substrate
98 by extending membrane processes, it is intuitive to hypothesize that a component of mechanosensing
99 is incorporated in the mechanism of cellular movement. The data above, on a critical role of Piezo1 in
100 migrating human T cells, also led us to hypothesize that Piezo1 mechanosensors may play a role in
101 sensing mechanical cues in a moving T cell. So, first we aimed at confirming that there is polarized
102 increase in tension in the leading edge plasma membrane of human T cells, moving in response to a
103 chemotactic cue.

104 Cellular membrane tension can be measured by various techniques. However, most of the usual
105 techniques, viz. atomic force microscopy or tension measurement using optical tweezers, are invasive
106 and interfere with the membrane dynamics, as well as are difficult to employ on moving cells. We
107 utilized the non-invasive technique of interference reflection microscopy or IRM for studying potential
108 redistribution of membrane tension following chemokine stimulation (32, 33). In IRM technique,
109 steady-state local fluctuations in the plasma membrane are imaged in cells adhered to a glass
110 coverslip. The interference patterns generated due to continuously changing local distance between
111 the coverslip and the plasma membrane are computed to derive the magnitude of local tension in the
112 membrane – lower temporal fluctuations represent an increase in membrane tension (Figure. 2A).
113 After baseline imaging, Piezo1-GFP expressing Jurkat cells were subjected to sequential fluorescence
114 and IRM imaging post SDF1α addition which was followed over time. Chemokine administration to
115 Jurkat T cells led to a decrease in temporal fluctuations and an increase in membrane tension when
116 computed for the whole cellular contour (Figure 2B). The increase in membrane tension was
117 registered within few minutes after chemokine addition and gradually declined over time (Figure 2C).
118 Distribution of tension and fluctuation-amplitude in cells was also affected by the action of chemokine
119 (Figure 2-figure supplement 1A) which was accompanied by increase in the membrane's degree of
120 confinement and the effective viscosity experienced (Figure 2-figure supplement 1C & D). Moreover,
121 the tension maps showed that the lamellipodial structures towards the leading edges of the cells had
122 higher tension magnitudes (Figure 2D, Figure 2-figure supplement 1B). These high-tension edges are
123 usually further emphasized at later time-points.

124 Finally, we explored if local membrane tension increase was linked to Piezo1 redistribution in the
125 chemokine-experienced T cells. Of note here, during acquisition, there is typically a time delay of 1
126 minute between measurement of tension and Piezo1-GFP fluorescence. As expected, average tension
127 peaked within the first few minutes of chemokine addition, followed by partial decline (Figure 2E) as
128 seen for the whole cell. Pixel count of Piezo1-GFP intensity showed a similar pattern, albeit, at a

129 delayed time, following the tension kinetics. In order to account for the delayed kinetics of tension
130 magnitude and Piezo1-GFP pixel count, we performed a correlation between normalised Piezo1 pixel
131 intensity at a particular time-frame, with normalised tension magnitude at the preceding time frame.
132 We observed significant positive correlation between the two cell-averaged parameters (Figure 2F,
133 G). This, however, does not capture the local spatial correlation between Piezo-1 intensity and tension.
134 Thus, IRM-coupled fluorescence microscopy revealed an increase in local membrane tension in the
135 leading edge of the moving T cells in response to chemokine receptor activation that was associated
136 with Piezo1 redistribution to the leading edges of the cells.

137

138 **Focal adhesion following chemokine receptor activation does not depend on Piezo1**

139 Focal adhesion formation is a critical step in cellular migration and activated phosphorylated focal
140 adhesion kinases link extracellular physical cues to the cytoskeletal actomyosin scaffold (34, 35).
141 Chemokine signaling induces phosphorylation of focal adhesion kinase (FAK) and membrane
142 recruitment of the FAK complex forming focal adhesions with the extracellular substrate. FAK recruits
143 adapter proteins like paxillin to anchor with the local sub-membrane cytoskeleton made by de novo
144 F-actin polymerization. Membrane-recruited FAK complexes anchored to cytoskeleton increases local
145 membrane tension as well as recruit integrins to the membrane (36, 6, 37). This so-called 'outside-in'
146 signaling, whereby membrane recruitment of integrins (e.g.; LFA1 in T cells) is initiated, is followed by
147 integrin signaling ('inside-out' signaling) driven primarily by phosphoinositide 3-kinase (PI3K)-driven
148 phosphorylation of Akt and downstream activation of Rho GTPases which in turn drive extensive F-
149 actin polymerization (38, 39). Retrograde flow of the F-actin to the rear end of the moving cells,
150 through myosin-based contractions, generates the propelling force for cells to move forward following
151 the chemokine gradient (6, 7).

152 Finding a critical role of Piezo1 in human T cell migration and a membrane tension-dependent
153 redistribution of Piezo1 to the leading edge of the moving cells led us explore if FAK recruitment to
154 the leading edge in response to chemokine stimulation was dependent on Piezo1. While
155 phosphorylated FAK (pFAK) showed striking polarity upon CCL19 stimulation on ICAM-1 beds (Figure
156 3A, B, Video 4), Piezo1 knockdown did not have any effect on pFAK polarity under the same conditions
157 (Figure 3C, D). We observed similar results upon examining distribution of paxillin which is another
158 critical component of focal adhesions. Paxillin showed increased polarity upon CCL19 stimulation
159 (Figure 3E, F) and its polarity remained unaffected upon Piezo1 KD (Figure 3G, H). We also did not
160 observe any changes in pFAK and paxillin signal intensity upon Piezo1 knockdown in CCL19-stimulated

161 cells (Figure 3-figure supplement 1A & B respectively). However, pFAK showed striking co-localization
162 with Piezo1 upon CCL19 stimulation (Figure 3-figure supplement 1C). Thus, focal adhesion formation
163 following chemokine receptor activation was not dependent on Piezo1. FAK activation recruits
164 adapters like paxillin and vinculin connecting the cortical cytoskeleton to the membrane and the
165 extracellular matrix, thereby increasing local membrane tension (34). Inhibition of FAK activation
166 completely abrogated Piezo1 redistribution to the leading edge, hence the polarity (Figure 3I, J). This
167 indicated that mechanistically, FAK activation event precedes Piezo1 redistribution to the leading edge
168 of the migrating human $CD4^+$ T cells.

169

170 **Membrane recruitment of LFA1 on chemokine receptor activation disrupts with Piezo1 deficiency**

171 Integrin recruitment to the leading edge occurs downstream of FAK activation and local F-actin
172 polymerization. As expected, CCL19 stimulation led to LFA1 recruitment to the leading edge upon
173 CCL19 stimulation on ICAM1 bed (Figure 4A, B; Video 5). Moreover, Piezo1 and LFA1 (CD11a) exhibited
174 significant colocalization upon chemokine stimulation (Figure 4C). Piezo1 downregulation abrogated
175 LFA-1 polarity (Figure 4D, E; Videos 6, 7). Thus, role of Piezo1 in chemotactic migration of T cells was
176 downstream of FAK assembly in response to chemokine receptor signaling, but preceded integrins
177 recruitment. These data together point to a mechanism whereby local increase in membrane tension
178 leading from FAK activation and assembly drives Piezo1 activation, which in turn is linked to LFA1
179 recruitment to the focal adhesions.

180 To further confirm this critical role of Piezo1 on LFA1 recruitment, we looked at the major signaling
181 event downstream of LFA1 recruitment to the leading edge, i.e., phosphorylation of Akt downstream
182 of PI3K activation, which in turn is triggered upon integrin activation. On treatment with CCL19, human
183 $CD4^+$ T cells moving on ICAM-1-coated plates did show a prominent leading-edge polarity of non-
184 phosphorylated and phosphorylated Akt (pAkt) (Figure 4F, control panel). But in Piezo1-deficient cells
185 the polarity of pAkt is abrogated (Figure 4G), not affecting the polarity of non-phosphorylated AKT
186 (Figure 4H; Videos 8, 9), substantiating the cellular signaling defect due to non-recruitment of LFA1 to
187 the leading edge membrane.

188 **Piezo1 deficiency disrupts F-actin retrograde flow in T cells despite chemokine receptor activation**

189 Piezo1-mediated sensing of membrane tension drives calcium ion influx, which in turn has been shown
190 to activate calpain and F-actin polymerization (14, 19). LFA1 recruitment is driven by local actin
191 scaffold formation following FAK assembly, which as our data indicates is perhaps contributed by
192 consolidation local actin scaffold downstream of Piezo1 activation. To confirm this, we performed Ca^{2+}

193 imaging in Piezo1-mCherry transfected Jurkat Cells using total internal reflection fluorescence (TIRF)
194 microscope in response to chemokine. We found significant colocalization of the Ca^{2+} signal with the
195 Piezo1 signal on the chemokine treated Jurkat cells (Figure 5A, B; Figure 5-figure supplement 1A & B).
196 Next to confirm that activation of calpain mediates the Piezo1 function, we observed that prior
197 inhibition with calpain inhibitor PD150606 abrogated CCL19-induced LFA1 recruitment to the leading
198 edge of the T cells (Figure 5C, D). As expected, the upstream event of pFAK polarity was not affected
199 by the calpain inhibition (Figure 5-figure supplement 1C & D).

200 While F-actin polymerization downstream of FAK is required for LFA1 recruitment, LFA1 in turn drives
201 a more robust F-actin polymerization at the leading edge, through Akt/Rho GTPase activation. Leading
202 edge F-actin undergoes retrograde flow due to myosin contractions, thereby enabling cells to move
203 forward. Thus, both at the leading edge lamellipodia and the rear edge F-actin redistribution can be
204 documented in a motile cell. We observed focal co-localization of LFA1 with F-actin at the leading
205 edge, along with a denser actin-rich protrusion in the rear edge or the uropod (Figure 5C), which was
206 abolished upon calpain inhibition (Figure 5C, E). Hence, LFA1 recruitment may depend on local F-actin
207 polarization downstream of Piezo1 activation. On the other hand, failure of LFA1 recruitment and
208 activation halts further F-actin polarization feeding the retrograde flow of actin during migration.

209 Dichotomy of Piezo1 (dense leading edge distribution) and F-actin (more dense at the rear end)
210 distribution was clearly demonstrated in cells stimulated with chemokine (Figure 6A and Video 10).
211 But, no F-actin polarity was seen on downregulating Piezo1 in the T cells (Figure 6B, C; Videos 11, 12).
212 Live cell imaging of Jurkat T cells expressing Piezo1-mCherry and actin-GFP on ICAM-1 coated dishes
213 was performed in the presence or absence of SDF1α (Figure 6-figure supplement 1A). Chemokine
214 addition showed significant increase in Piezo1 polarity to the front end, as shown in the earlier
215 experiments (Figure 6E, left Figure 6-figure supplement 1B, left) upon chemokine stimulation when
216 compared to untreated cells (Figure 6D, Figure 6-figure supplement 1B, left). But F-actin showed a
217 dynamic balance at both ends as expected (Figure 6E, Figure 6- figure supplement 1B, right). Polar
218 plots depicting angular distribution of Piezo1 mCherry and actin-GFP (over all time-points) in the
219 presence or absence of SDF1α are shown in Figure 6-figure supplement 1C. Representative image 6F
220 and Video 13 shows Piezo1-mCherry distribution predominantly at the leading edge and actin-GFP
221 eventually accumulating at the rear end in uropod-like cellular extensions in a migrating Jurkat T cell.

222 Thus, our data reveals a membrane-intrinsic event, involving a critical role of Piezo1 mechanosensors,
223 within the outside-in signaling module in response to chemokine receptor activation in human T cells.
224 The mechanistic model derived from our data is depicted in Figure 7. The Piezo1 mechanosensing links
225 the focal adhesion assembly to integrins recruitment at the leading edge of the human T cells

226 migrating in response to chemokine activation and thus play a critical role in chemotactic migration of
227 human T cells.

228

229 **DISCUSSION**

230 The present study explored the role of membrane-intrinsic tension generation and the crucial role of
231 sensing this physical cue in the context of human T cell migration in response to chemokine receptor
232 activation. Deficiency of Piezo1 inhibited integrin-dependent migration, demonstrating crucial role of
233 these mechanosensors in this mode of T cell migration. As the integrin-dependent chemotactic
234 migration of T cells is a critically implicated in most patho-physiologic contexts, in the present study
235 we focused on the potential role of Piezo1 mechanosensors in this specific context.

236 Notably, a previous study in vivo in mice, using genetic deletion of Piezo1 in T cells, reported no
237 significant effect on tissue recruitment of T cells (17). Although a functional redundancy in the role of
238 Piezo1-mediated mechanosensing in mouse T cells warrants exclusion, especially in case of gene
239 deletion in developing T cells, given the considerable expression of Piezo2 as well in mouse T cells (40).
240 On the other hand, a role of Piezo1 activation in fibroblastic reticular cells in Peyer's patches has been
241 shown to regulate lymphocyte migration through tissue conduits (41). The different tissue distribution
242 of Piezo1 and Piezo2 expression in humans warranted exploring the role of Piezo1 in migrating human
243 T cells, as in humans Piezo2 is hardly expressed in the hematopoietic cells.

244 Non-invasive interference reflection microscopy allowed us to demonstrate dynamic change in
245 membrane tension at the leading edge of T cells stimulated with chemokine on ICAM1-bed which was
246 closely followed by dynamic recruitment Piezo1 locally. Chemokine receptor activation leads to focal
247 adhesion formation at the leading edge of the migrating T cells (34, 35). Our experiments revealed
248 that Piezo1 recruitment at the leading edge of the cells followed focal adhesion kinase activation.
249 Focal adhesions do increase local membrane tension as they connect the extracellular environment
250 with the cortical cytoskeleton of the cell (34). Piezo1 recruitment locally seems to be a response to
251 this membrane tension increase at focal adhesions. Piezo1 recruitment to focal adhesions was also
252 shown to play a role in enhancing glioblastoma aggression by activating integrin-FAK signalling
253 upstream of ECM remodelling and tissue stiffening (42). Interestingly, recent study by Yao et. al.,
254 showed that Piezo1 is required for formation of mature focal adhesions. Piezo1 binds to matrix
255 adhesion regions in a force-dependent manner via a linker domain and this binding is abrogated in
256 cancer cells causing transformation to malignant phenotypes (43).

257 'Outside-in' signaling downstream of focal adhesion formation recruits integrins to the leading edge
258 of the moving T cells (35, 36) which was abrogated by Piezo1 downregulation. Piezo1 has been shown
259 to drive Ca^{2+} influx into the T cells leading to calpain activation (14, 19). As expected, calpain inhibition
260 also interfered with leading edge recruitment of the integrin LFA-1. Plausibly calpain activation drives
261 local F-actin polymerization at the leading edge facilitating LFA-1 recruitment. This was also supported
262 by loss of polarity of AKT phosphorylation with Piezo1 deficiency, which is known to be the major
263 downstream signaling module that succeeds LFA-1 recruitment and activation (39, 44). These
264 dysregulations in turn abrogates the retrograde flow of actin in the moving cell that is essential for
265 forward propulsion of the cell body (6, 7, 37, 43). Of note here, a role of ER-resident Piezo1, in driving
266 R-RAS-driven activation of integrins, which was again dependent on calpain activation, was reported
267 even before the mechanosensing function of Piezo1 was established (30).

268 Thus, the present study reports a hitherto unexplored role of the professional mechanosensor Piezo1
269 in integrin dependent chemotactic movement of human T cells. In the cascade of leading edge events
270 in a moving human T cell, following chemokine receptor activation and eventually leading to the
271 retrograde flow of actin, focal adhesion formation precedes Piezo1 activation, while LFA-1 recruitment
272 is dependent on Piezo1 function.

273

274 **MATERIALS AND METHODS**

275 **Human $CD4^+$ T cell isolation and transfection.**

276 Details of reagents used in the study are mentioned in Supplementary File 1.

277 Human $CD4^+$ T lymphocytes were isolated from peripheral blood from healthy donors through
278 magnetic immunoselection. Peripheral blood samples from healthy human subjects were collected on
279 obtaining written informed consents. The studies were approved by the Human Ethics Committee of
280 CSIR-Indian Institute of Chemical Biology, India. Cells were transfected with either EGFP control or
281 Piezo1-specific siRNAs using Lonza 4D nucleofector, as per the manufacturer's protocol. Briefly, cells
282 were nucleofected in 100µl of supplemented P3 primary buffer containing 175ng of respective siRNAs.
283 Nucleofection was performed using EO-115 pulse in Lonza 4D nucleofector. Nucleofected cells were
284 incubated at 37°C. 5% CO_2 in RPMI media containing 10% FBS for 3 days before experiments were
285 conducted. Knockdown was checked by qPCR measurement of Piezo1 and Piezo2 transcript levels
286 (Supplementary Figure. 1A).

287 GFP/Piezo1 siRNA co-nucleofection

288 Approximately 2×10^6 human CD4+ T lymphocytes were nucleofected with 3µg of GFP-expressing
289 plasmid along with 175ng of Piezo1-specific siRNA. Cells were incubated for 3 days before migration
290 studies. EGFP esiRNA was used as control siRNA in experiments involving comparison between control
291 and Piezo1 siRNA-KD cells.

292 Analysis of Piezo1 knockdown

293 GFP and Piezo1 siRNA co-transfected $CD4^+$ T cells were stained for Piezo1 to measure downregulation.
294 Both surface and intracellular (0.2% triton X-100 permeabilization) Piezo1 were stained. Briefly, cells
295 were collected on day and fixed in 0.5% PFA for 5 minutes on ice. Cells were stained with 1.67µg/ml
296 of rabbit anti-Piezo1 for 45 minutes at 4°C. After washing, 1.5µg/ml of anti-rabbit alexa 568-IgG was
297 added and incubated for 30 minutes at 4°C. Cells were acquired on BD LSR Fortessa III after washing.
298 Piezo1 mean fluorescence intensity (MFI) were measured both for GFP^+ and GFP^- cells. Paired t-test
299 was used to calculate statistical significance.

300 Quantitative PCR analysis of Piezo1 knockdown

301 Transfected $CD4^+$ T cells were analysed for Piezo1 knockdown using primers against human Piezo1 and
302 Piezo2. Primers specific for housekeeping gene, 18S was used to calculate the relative expression of
303 Piezo1 and Piezo2. Paired t-test was used to calculate statistical significance.

304 **2-dimensional cell tracking.**

305 12-mm confocal dishes were coated with 4µg/ml of recombinant human ICAM-1 overnight at 4°C.
306 Wells were washed with 1X PBS. Tracking of GFP/Piezo1 siRNA-transfected cells were performed after
307 cell trace violet-labelling in the presence of recombinant CCL19 on ICAM1-coated dishes. Stained cells
308 were added to the wells and allowed to settle for 1 hour at 37°C. 2D tracking was performed at 37°C
309 after addition of 0.5µg/ml of recombinant human CCL19 and incubated for 10 minutes before
310 acquisition. Images were acquired at regular intervals at room temperature using Zeiss LSM setup at
311 20X magnification for a total duration of 10-15 minutes at 30 second interval. $CD4^+$ T lymphocytes
312 were RPMI without phenol red supplemented with 10% FBS and 25mM HEPES during the duration of
313 imaging.

314 **2D cell tracking analysis**

315 For tracking analyses of GFP and Piezo1 siRNA co-transfected cells, all cells above a specific threshold
316 area were used to eliminate potential debris and dead cells due to GFP plasmid transfection. Time-
317 based image stacks obtained were analysed using the Particle Tracker 2D/3D plugin of the FIJI Mosaic
318 Suite. Briefly, images were corrected for any shift in alignment during acquisition, using the StackReg

319 plugin. Corrected images were the thresholded to create a 0-255 binary mask which were then used
320 for tracking using the Particle Tracker 2D/3D plugin. Tracking provided frame-wise X-Y co-ordinates
321 of cells which were subsequently used to derive the following parameter to measure motility:

322 *a. Mean-squared displacement*

323 *MSD (n)* = $\sum_{i=0}^{i=n}(x_n - x_0)^2 + (y_n - y_0)^2$ where,

324 i = 0 is the first frame,

325 i = n is the nth frame.

326 **Tranwell chemotaxis assay**

327 5µm transwell inserts were coated with 4µg/ml of recombinant human ICAM-1. Equal number of
328 primary human $CD4^+$ T cells and Jurkat cells nucleofected with control or Piezo1-specific siRNA were
329 added to the ICAM-1-coated inserts. Cells were allowed to migrate in response to recombinant human
330 CCL19 (0.5µg/ml) or SDF1α (0.1µg/ml) in the lower chamber wells for 5 hours and 1.5 hours,
331 respectively, at 37°C, 5% CO_2. Migration was halted by placing the setup on ice. Percent migration was
332 calculated by counting the number of cells in the lower chamber and dividing it by total number of
333 cells that was seeded.

334 **Overexpression of mCherry/GFP-tagged Piezo1 and Actin-GFP in Jurkat cells.**

335 GFP and mCherry-tagged Piezo1 constructs were kindly provided by Dr. Charles Cox at Victor Chang
336 Cardiac Research Laboratory, Darlinghurst, Australia. Approximately 2 million Jurkat cells were
337 nucleofected with 2-3µg of fluorescent Piezo1 construct in 100µl of supplemented SE cell line buffer.
338 Cells were pulsed using CL-120 program in Lonza 4D nucleofector. Cells were cultured in antibiotics-
339 deficient RPMI supplemented with 20% FBS for 36 hours. Overexpression was confirmed using flow
340 cytometry.

341 **Interference Reflection Microscopy and Analysis**

342 Jurkat cells were nucleofected with 2-3µg/ml of Piezo1-GFP construct. Overexpression was confirmed
343 using flow cytometry. Transfected cells were seeded on recombinant human fibronectin glass-based
344 dishes. Cells were allowed to completely adhere for 1 hour to allow IRM imaging.

345 An inverted microscope (Nikon, Japan) with 60x 1.2 NA water-immersion objective, Hg arc lamp and
346 necessary interference filter (546 ± 12 nm) were used for the interference reflection microscopy (45,
347 46) and images were captured at 19.91 frames per second using a EMCCD camera (Evolve 512 Delta;

348 Photometrics, Trenton, NJ). Cells that were significantly adhered to the glass bottom were used for
349 imaging. Regions used for analysis were stringently chosen to avoid parts farther than ~ 100 nm from
350 the coverslip – also called the first branch region (FBR) and the size chosen was 4x4 pixels
351 corresponding to ~ $(720\ nm)^2$. First, cells were imaged by IRM to take baseline reading following which
352 chemokine (SDF1α) was added. Cells were followed till 30 min with ~ 2-3 min interval post-chemokine
353 addition.

354 For stringent selection of subset of regions, extraction of parameters as well as for visualizing the
355 amplitude of fluctuations, the methodology developed previously (46, 47) was followed. 2048 frames
356 corresponding to ~ 102 sec were captured and used for a single measurement of tension. The analysis
357 involved calculation of standard deviation of temporal height fluctuations (SD_{time}) and estimating the
358 power spectral density (PSD) by autoregressive technique (probability of covariance or pcov) where
359 the order is chosen to match best with PSD obtained using fast fourier transform (MATLAB, Mathworks
360 Inc., USA). For deriving mechanical parameters, the PSD is fitted with a Helfrich-based model –

361 $$PSD(f) = \frac{4\eta_{eff} A k_B T}{\pi} \int_{q_{min}}^{q_{max}} \frac{dq}{(4\eta_{eff}(2\pi f))^2 + \left[\kappa q^3 + \sigma q + \frac{\gamma}{q}\right]^2}$$

362 with four fitting parameters (46) using fluctuation-tension (σ), effective viscosity (η_{eff}), level of
363 confinement (γ) and the effective active temperature (*A*)). The bending rigidity (κ) was fixed at 15 k_BT.
364 Membrane fluctuation-tension closely follows membrane frame tension for a large range of tension
365 values (48). Membrane fluctuation-tension closely follows membrane frame tension for a large range
366 of tension values (48). For brevity, membrane fluctuation-tension has been referred to as "tension" in
367 the rest of the manuscript. Tension maps were created from PSDs calculated for every pixel which
368 were subsequently fitted and parameters extracted for every pixel. For analysing correlation between
369 fluorescence and tension, first the fluorescence distribution of cells was plotted. Regions of
370 intermediate intensity (around the first peak of the distribution) of a fixed intensity range was filtered
371 and the pixel count of the filtered area was plotted against the average tension in those pixels.
372 Normalization was done by diving by the maximum value in the time series. Normalized pixel count,
373 thus, reflects how area with high Piezo1-GFP at the membrane changes while avoiding a small area
374 fraction with very high Piezo1-GFP which might arise from internal structures. To ensure significance
375 of the observed differences, the statistical test undertaken was the Mann-Whitney U test with
376 Bonferroni correction.

377 **Piezo1 and actin distribution in live cell imaging**

378 Jurkat cells expressing mCherry-tagged Piezo1 were seeded on ICAM-1-coated dishes. 0.1µg/ml of
379 recombinant human SDF1α was added to the cells for 15 minutes prior to imaging. Cell tracking was
380 performed in EVOS FL microscope using the PE-Texas red filter, at an interval of 1 frame per minute,
381 at room temperature. Imaging was performed for a total duration of 15 minutes.

382 For Jurkat cells transfected with Piezo1-mcherry and actin-GFP, cells were treated similarly and
383 acquired on Zeiss LSM confocal setup. Z-stack was obtained at 1µm per stack to capture the entire
384 cell. Time-lapse was imaged at an interval of 30 second per frame for a total duration of 5 minutes.
385 Confocal imaging was performed at 37°C.

386 For particle image velocimetry (PIV) analysis of Piezo1-mCherry-expressing Jurkat cells was performed
387 using the Iterative PIV plugin of FIJI. Time-lapse image stacks were split and stacks of paired
388 subsequent images were formed. Each of these stacks was then corrected for any shift in alignment
389 using the StackReg plugin. Aligned stacks were then subjected to iterative FIJI PIV analysis using the
390 conventional cross-correlation method to measure flow of fluorescent Piezo1 in chemokine-treated
391 Jurkat cells. PIV post-processing was done with default parameters and PIV magnitude plots were
392 obtained from the plugin.

393 **Measurement of cell polarity during live-cell imaging.**

394 A custom code was written in Fiji (ImageJ) to analyze the cell image time-lapse for the calculation
395 Front/Back (F/B) ratio of actin and Piezo1 expression relative to the direction of cell migration. Briefly,
396 intensity-based thresholding was performed on the actin images to create binary masks of the cells.
397 Individual cell boundaries were identified in the time-lapse, which were stored in the form of polygon
398 ROIs. The cell ROIs enabled the computation of each cell's trajectory and displacement vectors from
399 the geometrical centroid at every frame of the time-lapse video. The computation of cell polarity
400 involved fitting each cell’s ROI to an ellipse and bisecting the ellipse perpendicular to the migration
401 direction. The ratio of total intensities in the leading half and the trailing half of the ellipse was
402 calculated for actin and piezo1 images to get the F/B ratio.

403 For polarity measurement of fixed confocal images, cell boundaries were similarly identified. Stored
404 ROIs were then split into two halves perpendicular to the long axis of the cell. The polarity index was
405 measured by calculating the difference of total intensities of two halves of the cell divided by the sum
406 of their total intensities. A measurement of 1 shows complete skewing of fluorescent signals to one
407 half of the cell, while a value of 0 shows uniform distribution of fluorescent signals in both cell halves
408 Representative polarity analysis Piezo1 (fixed), Piezo1 mCherry (live), pFAK (fixed), CD11a/LFA-1

409 (fixed) and actin (fixed) of untreated and CCL19-stimulated $CD4^+$ T lymphocytes (Methods-figure
410 supplement 1).

411 For measuring relative polarity of CD44 and Piezo1, polarity measurement was performed using Fiji as
412 mentioned above. To enable comparison of Piezo1 polarity relative to CD44 polarity, polarity indices
413 $[\frac{intensity\ of\ cell\ halves\ (A-B)}{intensities\ of\ cell\ halves\ (A+B)}]$ were calculated so as to assign a positive difference, hence polarity, to
414 CD44 (intensity of CD44 in A>B). The same order was used to calculate polarity index of Piezo1. If CD44
415 and Piezo1 polarize to the same cell half, then both polar indices will be positive. If, however, Piezo1
416 polarises to the opposite pole, it will show a negative polarity index with respect to CD44. Paired t-
417 test was used to calculate statistical significance.

418 **Generation of Piezo1 mCherry and Actin-GFP polar plots.**

419 For analysis of angular/spatial distribution of Piezo1 mCherry and actin-GFP with respect to direction
420 of cell movement, cell ROIs were applied to the actin and piezo1 channels individually, to find the
421 intensity-weighted centre of mass (through all the time-points). Depending on the fluorescence
422 intensity distribution, the intensity-weighted centre of mass is shifted away from the geometric
423 centroid and towards the direction of a higher protein distribution. Thus, a vector connecting the
424 centroid (geometric centre) to the centre of mass gives the direction of polarization of the protein of
425 interest. The relative angle of the polarization vector against the cell displacement vector was
426 calculated for each frame, and a polar histogram of the angles was plotted for actin-GFP and piezo1-
427 mCherry.

428 **Fixed immunostaining for confocal imaging**

429 Untransfected human $CD4^+$ T lymphocytes were seeded on 12-mm, ICAM-1-coated glass coverslips at
430 a density of about 0.2 million cells per coverslip. Cells were incubated at 37°C, 5% CO_2 for 1.5 hours.
431 0.5µg/ml of recombinant human CCL19 was added to each coverslip and incubated for 20-30 minutes
432 at 37°C. Post-treatment, cells were fixed in 4% paraformaldehyde for 15 minutes at room
433 temperature. Blocking was performed in 3% bovine serum albumin in 1X PBS containing 0.2% Triton
434 X-100 for 50 minutes at room temperature. Primary rabbit anti-human Piezo1 (Proteintech) was
435 added at a dilution of 1:100 (5µg/ml) and incubated at room temperature for 1 to 1.5 hours. Alexa
436 568-conjugated anti-rabbit IgG was added at a dilution of 1:350 (5.7µg/ml), and incubated for further
437 45-50 minutes. Nuclear staining was performed for 1 minute with Hoechst 33342 dye at a
438 concentration of 1µg/ml in 1X PBS. All washes between steps were carried out in 1X PBS. Stained cells
439 were then mounted on Vectashield® mounting media and sealed before confocal imaging. For Piezo1
440 and CD44 co-staining, rabbit anti-Piezo1 and mouse anti-human CD44 were used at a concentration

441 of 5µg/ml, each. Alexa 488-conjugated anti-rabbit IgG and alexa 633-conjugated anti-mouse IgG were
442 used at a concentration of 5.7µg/ml, each.

443 For actin imaging, LifeAct-TagGFP2 protein was added at a concentration of 0.5µg/ml, and incubated
444 for 45 minutes at room temperature before washing. For LFA-1 ($\alpha_L\beta2$) and actin co-staining, mouse
445 anti-human CD11a (α_L subunit) was added at a concentration of 5µg/ml, followed by addition of anti-
446 mouse Alexa 488-conjugated IgG and Alexa fluor 532 tagged-phalloidin. For LFA-1 and Piezo1 co-
447 staining, primary antibodies were added at above concentrations, with Alexa 568-conjugated anti-
448 rabbit IgG (for Piezo1) and Alexa 488-conjuagted anti-mouse IgG (for CD11a/LFA-1). Rabbit/mouse
449 anti-phosphorylated FAK (Tyr-397) and mouse Paxillin was used to stain pFAK and paxillin, respectively
450 to detect focal adhesions. These cells were treated with chemokine CCL19 for 10 minutes prior to
451 fixation. While doing confocal microscopy, Z-stacks were captured at 0.5µm intervals. Confocal images
452 are represented are maximum intensity projections of the Z-slices. 3Dprojectionfunction of Fiji was
453 used to create a 3D rendering of the Z-slices, using the brightest point method of projection.

454 **TIRF Imaging and Ca^{2+}-Piezo1 colocalization**

455 Ca^{2+}-Piezo1 imaging involved incubating cells with Fluo-3 AM (2.5 µM) in HBSS buffer for 30 minutes
456 at 37˚C, followed by washing and imaging in RPMI containing 10% FBS, and 25 mM HEPES media.
457 Jurkat cell were transfected with Piezo1 mCherry plasmid and only those expressing Piezo1 mCherry
458 were selected for the study. Dual-colour sequential TIRF imaging was employed, with Piezo1 mCherry
459 being imaged at 300 ms (100 frames) and Ca2+ imaging performed using a 10 ms exposure time (2000
460 frames). The short exposure for Ca2+ was used to capture transient local peaks of fluorescence which
461 would otherwise average out at longer exposure times. The maximum projection of the time series
462 was used to detect local peaks using adaptive local thresholding (MATLAB), and a size filter was used
463 to exclude large objects identified with a relatively low Ca^{2+} gradient. For each specific set of settings,
464 the Ca^{2+} signal objects detected were used to calculate the average cluster size and total area of
465 objects. Uniform random numbers were used to simulate clusters with appropriate probability to
466 ensure that the final area of the simulated Ca^{2+} clusters closely matched the real data. The overlap
467 between the real Ca^{2+} signal and Piezo1 objects was compared with the simulated data to test for
468 deviation from a random placement of Ca^{2+} spots. To assess the robustness of the results, different
469 combinations of size filters of Piezo1 and Ca^{2+} objects were used, ranging from 50 to 350 pixels.

470 **Calpain Inhibition**

471 PD150606 (Merck, India), a non-competitive calpain 1 and 2 inhibitors, was used at a concentration of
472 100µM. Untransfected $CD4^+$ T lymphocytes were treated with PD150606 for 1 hour at 37°C prior to
473 treatment of chemokine. Post -chemokine treatment cells were stained either with pFAK as described.

474 **Focal adhesion kinase Inhibition**

475 FAK inhibitor 14 (1,2,4,5-Benzenetetraamine tetrahydrochloride) was used to selectively inhibit FAK
476 activity. Inhibitor was added at a final concentration 10µM, 1 hour prior to treatment with
477 recombinant CCL19. Post-treatment with CCL19, $CD4^+$ T lymphocytes were stained with Piezo1 for
478 confocal imaging.

479 **Piezo1 Inhibition**

480 Primary human $CD4^+$ T cells were incubated with 10µM of GsMTx4 for 1 hour prior to transwell
481 chemotaxis assay in response to recombinant CCL19. Paired t-test was used to calculate statistical
482 significance.

483 **Statistics**

484 Student t-test was used to calculate significance, unless specified. $p<0.05$ was considered to be
485 statistically significant.

486 **Data availability**

487 All data included in the study has been uploaded as Supplementary File 2. Codes used for imaging are
488 provided in Supplementary File 3.

489

490 **ACKNOWLEDGEMENTS**

491 The study was funded by Council of Scientific and Industrial Research, India (Grant no. FBR MLP-140).
492 D.G. is a recipient of Swarnajayanti Fellowship from Department of Science and Technology,
493 Government of India. The authors express their gratitude for provision of the Piezo1 constructs by Dr.
494 Charles Cox, Victor Chang Institute of Cardiac Research, Australia.

495

496 **REFERENCES**

497 1. Shechter R, London A, Schwartz M. Orchestrated leukocyte recruitment to immune-privileged
498 sites: absolute barriers versus educational gates. Nat Rev Immunol. 2013 Mar;13(3):206-18.
499 doi: 10.1038/nri3391.
500 2. Krummel MF, Bartumeus F, Gérard A. T cell migration, search strategies and mechanisms. Nat
501 Rev Immunol. 2016 Mar;16(3):193-201. doi: 10.1038/nri.2015.16.
502 3. Woodland DL, Kohlmeier JE. Migration, maintenance and recall of memory T cells in peripheral
503 tissues. Nat Rev Immunol. 2009 Mar;9(3):153-61. doi: 10.1038/nri2496.
504 4. Masopust D, Schenkel JM. The integration of T cell migration, differentiation and function. Nat
505 Rev Immunol. 2013 May;13(5):309-20. doi: 10.1038/nri3442.
506 5. Fowell DJ, Kim M. The spatio-temporal control of effector T cell migration. Nat Rev Immunol.
507 2021 Sep;21(9):582-596. doi: 10.1038/s41577-021-00507-0.
508 6. Dupré L, Houmadi R, Tang C, Rey-Barroso J. T Lymphocyte Migration: An Action Movie Starring
509 the Actin and Associated Actors. Front Immunol. 2015 Nov 18;6:586. doi:
510 10.3389/fimmu.2015.00586.
511 7. Nordenfelt P, Moore TI, Mehta SB, Kalappurakkal JM, Swaminathan V, Koga N, Lambert TJ,
512 Baker D, Waters JC, Oldenbourg R, Tani T, Mayor S, Waterman CM, Springer TA. Direction of
513 actin flow dictates integrin LFA-1 orientation during leukocyte migration. Nat Commun. 2017
514 Dec 11;8(1):2047. doi: 10.1038/s41467-017-01848-y.
515 8. Moreau HD, Piel M, Voituriez R, Lennon-Duménil AM. Integrating Physical and Molecular
516 Insights on Immune Cell Migration. Trends Immunol. 2018 Aug;39(8):632-643. doi:
517 10.1016/j.it.2018.04.007.
518 9. Shannon MJ, Pineau J, Griffié J, Aaron J, Peel T, Williamson DJ, Zamoyska R, Cope AP, Cornish
519 GH, Owen DM. Differential nanoscale organisation of LFA-1 modulates T-cell migration. J Cell
520 Sci. 2019 Oct 16;133(5):jcs232991. doi: 10.1242/jcs.232991.
521 10. Coste B, Mathur J, Schmidt M, Earley TJ, Ranade S, Petrus MJ, Dubin AE, Patapoutian A. Piezo1
522 and Piezo2 are essential components of distinct mechanically activated cation channels.
523 Science. 2010 Oct 1;330(6000):55-60. doi: 10.1126/science.1193270.
524 11. Coste B, Xiao B, Santos JS, Syeda R, Grandl J, Spencer KS, Kim SE, Schmidt M, Mathur J, Dubin
525 AE, Montal M, Patapoutian A. Piezo proteins are pore-forming subunits of mechanically
526 activated channels. Nature. 2012 Feb 19;483(7388):176-81. doi: 10.1038/nature10812.
527 12. Syeda R, Florendo MN, Cox CD, Kefauver JM, Santos JS, Martinac B, Patapoutian A. Piezo1
528 Channels Are Inherently Mechanosensitive. Cell Rep. 2016 Nov 8;17(7):1739-1746. doi:
529 10.1016/j.celrep.2016.10.033.

530 13. Murthy SE, Dubin AE, Patapoutian A. Piezos thrive under pressure: mechanically activated ion
531 channels in health and disease. Nat Rev Mol Cell Biol. 2017 Dec;18(12):771-783. doi:
532 10.1038/nrm.2017.92. Epub 2017 Oct 4. PMID: 28974772.
533 14. Liu CSC, Raychaudhuri D, Paul B, Chakrabarty Y, Ghosh AR, Rahaman O, Talukdar A, Ganguly
534 D. Cutting Edge: Piezo1 Mechanosensors Optimize Human T Cell Activation. J Immunol. 2018
535 Feb 15;200(4):1255-1260. doi: 10.4049/jimmunol.1701118.
536 15. Atcha H, Jairaman A, Holt JR, Meli VS, Nagalla RR, Veerasubramanian PK, Brumm KT, Lim HE,
537 Othy S, Cahalan MD, Pathak MM, Liu WF. Mechanically activated ion channel Piezo1
538 modulates macrophage polarization and stiffness sensing. Nat Commun. 2021 May
539 31;12(1):3256. doi: 10.1038/s41467-021-23482-5.
540 16. Geng J, Shi Y, Zhang J, Yang B, Wang P, Yuan W, Zhao H, Li J, Qin F, Hong L, Xie C, Deng X, Sun
541 Y, Wu C, Chen L, Zhou D. TLR4 signalling via Piezo1 engages and enhances the macrophage
542 mediated host response during bacterial infection. Nat Commun. 2021 Jun 10;12(1):3519. doi:
543 10.1038/s41467-021-23683-y.
544 17. Jairaman A, Othy S, Dynes JL, Yeromin AV, Zavala A, Greenberg ML, Nourse JL, Holt JR, Cahalan
545 SM, Marangoni F, Parker I, Pathak MM, Cahalan MD. Piezo1 channels restrain regulatory T
546 cells but are dispensable for effector CD4+ T cell responses. Sci Adv. 2021 Jul
547 7;7(28):eabg5859. doi: 10.1126/sciadv.abg5859.
548 **18.** Jäntti H, Sitnikova V, Ishchenko Y, Shakirzyanova A, Giudice L, Ugidos IF, Gómez-Budia M,
549 Korvenlaita N, Ohtonen S, Belaya I, Fazaludeen F, Mikhailov N, Gotkiewicz M, Ketola K,
550 Lehtonen Š, Koistinaho J, Kanninen KM, Hernández D, Pébay A, Giugno R, Korhonen P,
551 Giniatullin R, Malm T. Microglial amyloid beta clearance is driven by PIEZO1 channels. J
552 Neuroinflammation. 2022 Jun 15;19(1):147. doi: 10.1186/s12974-022-02486-y.
553 19. Liu CSC, Ganguly D. Mechanical Cues for T Cell Activation: Role of Piezo1 Mechanosensors.
554 Crit Rev Immunol. 2019;39(1):15-38. doi: 10.1615/CritRevImmunol.2019029595.
555 20. Ma S, Dubin AE, Zhang Y, Mousavi SAR, Wang Y, Coombs AM, Loud M, Andolfo I, Patapoutian
556 A. A role of PIEZO1 in iron metabolism in mice and humans. Cell. 2021 Feb 18;184(4):969-
557 982.e13. doi: 10.1016/j.cell.2021.01.024.
558 21. He Y, Deng B, Liu S, Luo S, Ning Y, Pan X, Wan R, Chen Y, Zhang Z, Jiang J, Xu H, Xia M, Li J.
559 Myeloid Piezo1 Deletion Protects Renal Fibrosis by Restraining Macrophage Infiltration and
560 Activation. Hypertension. 2022 May;79(5):918-931. doi:
561 10.1161/HYPERTENSIONAHA.121.18750.

562 22. Huang Z, Sun Z, Zhang X, Niu K, Wang Y, Zheng J, Li H, Liu Y. Loss of stretch-activated channels,
563 PIEZOs, accelerates non-small cell lung cancer progression and cell migration. Biosci Rep. 2019
564 Mar 22;39(3): BSR20181679. doi: 10.1042/BSR20181679.
565 23. Chubinskiy-Nadezhdin VI, Vasileva VY, Vassilieva IO, Sudarikova AV, Morachevskaya EA,
566 Negulyaev YA. Agonist-induced Piezo1 activation suppresses migration of transformed
567 fibroblasts. Biochem Biophys Res Commun. 2019 Jun 18;514(1):173-179. doi:
568 10.1016/j.bbrc.2019.04.139.
569 24. Mousawi F, Peng H, Li J, Ponnambalam S, Roger S, Zhao H, Yang X, Jiang LH. Chemical
570 activation of the Piezo1 channel drives mesenchymal stem cell migration via inducing ATP
571 release and activation of P2 receptor purinergic signaling. Stem Cells. 2020 Mar;38(3):410-
572 421. doi: 10.1002/stem.3114.
573 25. Wang X, Cheng G, Miao Y, Qiu F, Bai L, Gao Z, Huang Y, Dong L, Niu X, Wang X, Li Y, Tang H, Xu
574 Y, Song X. Piezo type mechanosensitive ion channel component 1 facilitates gastric cancer
575 omentum metastasis. J Cell Mol Med. 2021 Feb;25(4):2238-2253. doi: 10.1111/jcmm.16217.
576 26. Gao L, Ji Y, Wang L, He M, Yang X, Qiu Y, Sun X, Ji Z, Yang G, Zhang J, Li S, Dai L, Zhang L.
577 Suppression of Esophageal Squamous Cell Carcinoma Development by Mechanosensitive
578 Protein Piezo1 Downregulation. ACS Omega. 2021 Apr 12;6(15):10196-10206. doi:
579 10.1021/acsomega.1c00505.
580 27. Holt JR, Zeng WZ, Evans EL, Woo SH, Ma S, Abuwarda H, Loud M, Patapoutian A, Pathak MM.
581 Spatiotemporal dynamics of PIEZO1 localization controls keratinocyte migration during
582 wound healing. Elife. 2021 Sep 27;10:e65415. doi: 10.7554/eLife.65415.
583 28. Velasco-Estevez M, Koch N, Klejbor I, Caratis F, Rutkowska A. Mechanoreceptor Piezo1 Is
584 Downregulated in Multiple Sclerosis Brain and Is Involved in the Maturation and Migration of
585 Oligodendrocytes in vitro. Front Cell Neurosci. 2022 May 26;16:914985. doi:
586 10.3389/fncel.2022.914985.
587 29. Hung WC, Yang JR, Yankaskas CL, Wong BS, Wu PH, Pardo-Pastor C, Serra SA, Chiang MJ, Gu
588 Z, Wirtz D, Valverde MA, Yang JT, Zhang J, Konstantopoulos K. Confinement Sensing and Signal
589 Optimization via Piezo1/PKA and Myosin II Pathways. Cell Rep. 2016 May 17;15(7):1430-1441.
590 doi: 10.1016/j.celrep.2016.04.035.
591 30. McHugh BJ, Buttery R, Lad Y, Banks S, Haslett C, Sethi T. Integrin activation by Fam38A uses a
592 novel mechanism of R-Ras targeting to the endoplasmic reticulum. J Cell Sci. 2010 Jan 1;123(Pt
593 1):51-61. doi: 10.1242/jcs.056424.

31. Xiao B. 2020. Levering Mechanically Activated Piezo Channels for Potential Pharmacological Intervention. Annu Rev PharmacolToxicol. 60:195-218. doi: 10.1146/annurev-pharmtox-010919-023703.
32. Barr VA, Bunnell SC. Interference reflection microscopy. Curr Protoc Cell Biol. 2009 Dec; Chapter 4: Unit 4.23. doi: 10.1002/0471143030.cb0423s45.
33. Chakraborty M, Mukherjee B, Nalinakshan N, Biswas A, Nayak RK, Sinha B. Effect of heterogeneous substrate adhesivity of follower cells on speed and tension profile of leader cells in primary keratocyte collective cell migration. Biol Open. 2022 Mar 15;11(3):bio058893. doi: 10.1242/bio.058893.
34. Mitra SK, Hanson DA, Schlaepfer DD. Focal adhesion kinase: in command and control of cell motility. Nat Rev Mol Cell Biol. 2005 Jan;6(1):56-68. doi: 10.1038/nrm1549.
35. Katoh K. FAK-Dependent Cell Motility and Cell Elongation. Cells. 2020 Jan 12;9(1):192. doi: 10.3390/cells9010192.
36. Yamashiro S, Watanabe N. A new link between the retrograde actin flow and focal adhesions. J Biochem. 2014 Nov;156(5):239-48. doi: 10.1093/jb/mvu053.
37. Martino F, Perestrelo AR, Vinarský V, Pagliari S, Forte G. Cellular Mechanotransduction: From Tension to Function. Front Physiol. 2018 Jul 5;9:824. doi: 10.3389/fphys.2018.00824.
38. Sánchez-Martín L, Sánchez-Sánchez N, Gutiérrez-López MD, Rojo AI, Vicente-Manzanares M, Pérez-Alvarez MJ, Sánchez-Mateos P, Bustelo XR, Cuadrado A, Sánchez-Madrid F, Rodríguez-Fernández JL, Cabañas C. Signaling through the leukocyte integrin LFA-1 in T cells induces a transient activation of Rac-1 that is regulated by Vav and PI3K/Akt-1. J Biol Chem. 2004 Apr 16;279(16):16194-205. doi: 10.1074/jbc.M400905200.
39. Roy NH, Kim SHJ, Buffone A Jr, Blumenthal D, Huang B, Agarwal S, Schwartzberg PL, Hammer DA, Burkhardt JK. LFA-1 signals to promote actin polymerization and upstream migration in T cells. J Cell Sci. 2020 Sep 9;133(17):jcs248328. doi: 10.1242/jcs.248328.
40. Ganguly D. Can Piezo2 substitute Piezo1 function in the context of T cell-specific deletion in mice? Sci Adv, e-Letter published Sep 8, 2021, in response to Jairaman A et al.,
41. Chang JE, Buechler MB, Gressier E, Turley SJ, Carroll MC. Mechanosensing by Peyer's patch stroma regulates lymphocyte migration and mucosal antibody responses. Nat Immunol. 2019 Nov;20(11):1506-1516. doi: 10.1038/s41590-019-0505-z.
42. Chen X, Wanggou S, Bodalia A, Zhu M, Dong W, Fan JJ, Yin WC, Min HK, Hu M, Draghici D, Dou W, Li F, Coutinho FJ, Whetstone H, Kushida MM, Dirks PB, Song Y, Hui CC, Sun Y, Wang LY, Li X, Huang X. A Feedforward Mechanism Mediated by Mechanosensitive Ion Channel PIEZO1 and Tissue Mechanics Promotes Glioma Aggression. Neuron. 2018 Nov 21;100(4):799-815.e7.

628 43. Yao M, Tijore A, Cheng D, Li JV, Hariharan A, Martinac B, Tran Van Nhieu G, Cox CD, Sheetz M.
629 Force- and cell state-dependent recruitment of Piezo1 drives focal adhesion dynamics and
630 calcium entry. Sci Adv. 2022 Nov 11;8(45):eabo1461.
631 44. Roy NH, MacKay JL, Robertson TF, Hammer DA, Burkhardt JK. Crk adaptor proteins mediate
632 actin-dependent T cell migration and mechanosensing induced by the integrin LFA-1. Sci
633 Signal. 2018 Dec 11;11(560):eaat3178. doi: 10.1126/scisignal.aat3178.
634 45. Limozin L, Sengupta K. Quantitative reflection interference contrast microscopy (RICM) in soft
635 matter and cell adhesion. Chemphyschem. 2009 Nov 9;10(16):2752-68.
636 46. Biswas A, Alex A, Sinha B. Mapping Cell Membrane Fluctuations Reveals Their Active
637 Regulation and Transient Heterogeneities. Biophys J. 2017 Oct 17;113(8):1768-1781. doi:
638 10.1016/j.bpj.2017.08.041.
639 47. Biswas A, Kashyap P, Datta S, Sengupta T, Sinha B. Cholesterol Depletion by MβCD Enhances
640 Cell Membrane Tension and Its Variations-Reducing Integrity. Biophys J. 2019 Apr
641 23;116(8):1456-1468.
642 48. Shiba H, Noguchi H, Fournier JB. Monte Carlo study of the frame, fluctuation and internal
643 tensions of fluctuating membranes with fixed area. Soft Matter. 2016 Feb 28;12(8):2373-80.
644 doi: 10.1039/c5sm01900a.

645

646

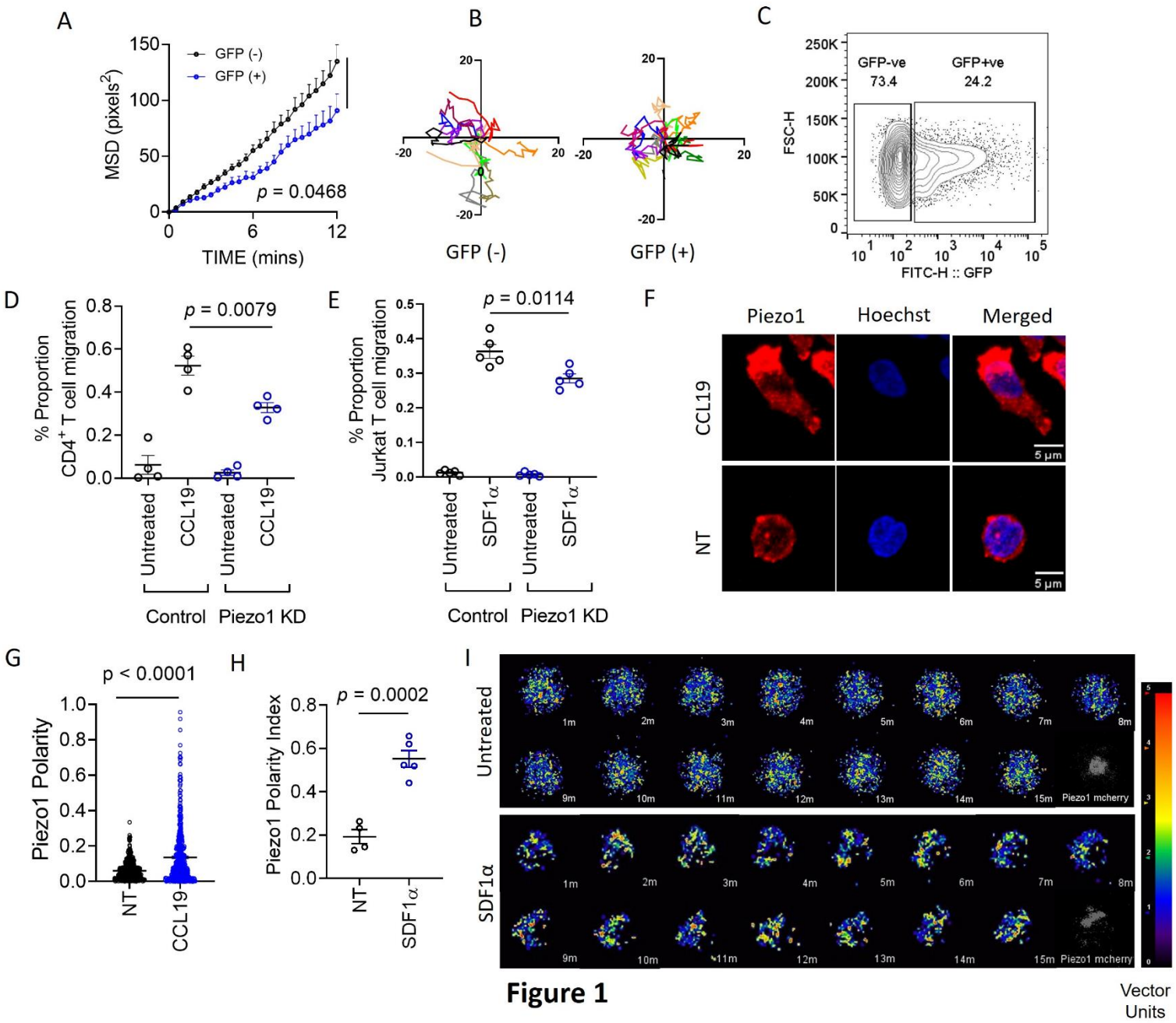

Figure 1

Figure 1. Piezo1 deficiency abrogates integrin-dependent motility in human T cells which is mediated through redistribution of Piezo1 at the leading edge in response to chemokine stimulation.

A. MSD versus time calculated for GFP⁺ (potential Piezo1-knockdown cells) and GFP⁻ (potential control cells) in GFP plasmid and Piezo1 siRNA co-transfected human CD4⁺ T lymphocytes, that were allowed to migrate in presence of recombinant CCL19 on ICAM1-coated dishes. **B.** Representative tracks of GFP⁺ and GFP⁻ CD4⁺ T lymphocytes. Comparisons of **C.** % GFP⁺ cells after 72 hours of nucleofection **D**

655 **& E.** 3D transwell migration assay of siRNA-transfected primary human $CD4^+$ T lymphocytes (D) and
656 Jurkat T cells (E), respectively. Data representative of at least 3 independent experiments. **F.**
657 Representative confocal images of Piezo1 distribution in fixed untreated and CCL19-treated $CD4^+$ T
658 lymphocytes. 63X oil magnification. **G.** Comparison between Piezo1 polarity index calculated for fixed,
659 stained, human $CD4^+$ T lymphocytes with or without 0.5µg/ml CCL19 treatment for 20-30 minutes. n
660 > 510 random cells, each. **H.** Piezo1 polarity index calculated for Jurkat cells, expressing mCherry-
661 tagged Piezo1 during live-cell tracking in the presence of recombinant SDF1α. Each dot represents
662 polarity index of each cell, averaged over all the time-frames. **I.** Representative time kinetics of particle
663 image velocimetry (PIV) analysis of Piezo1-mcherry transfected Jurkat cells, allowed to move on ICAM-
664 coated dishes in the presence of recombinant SDF1α. Top panel: No chemokine. Bottom Panel: SDF1α.

665

666

667

668

669

670

671

672

673

674

675

676

677

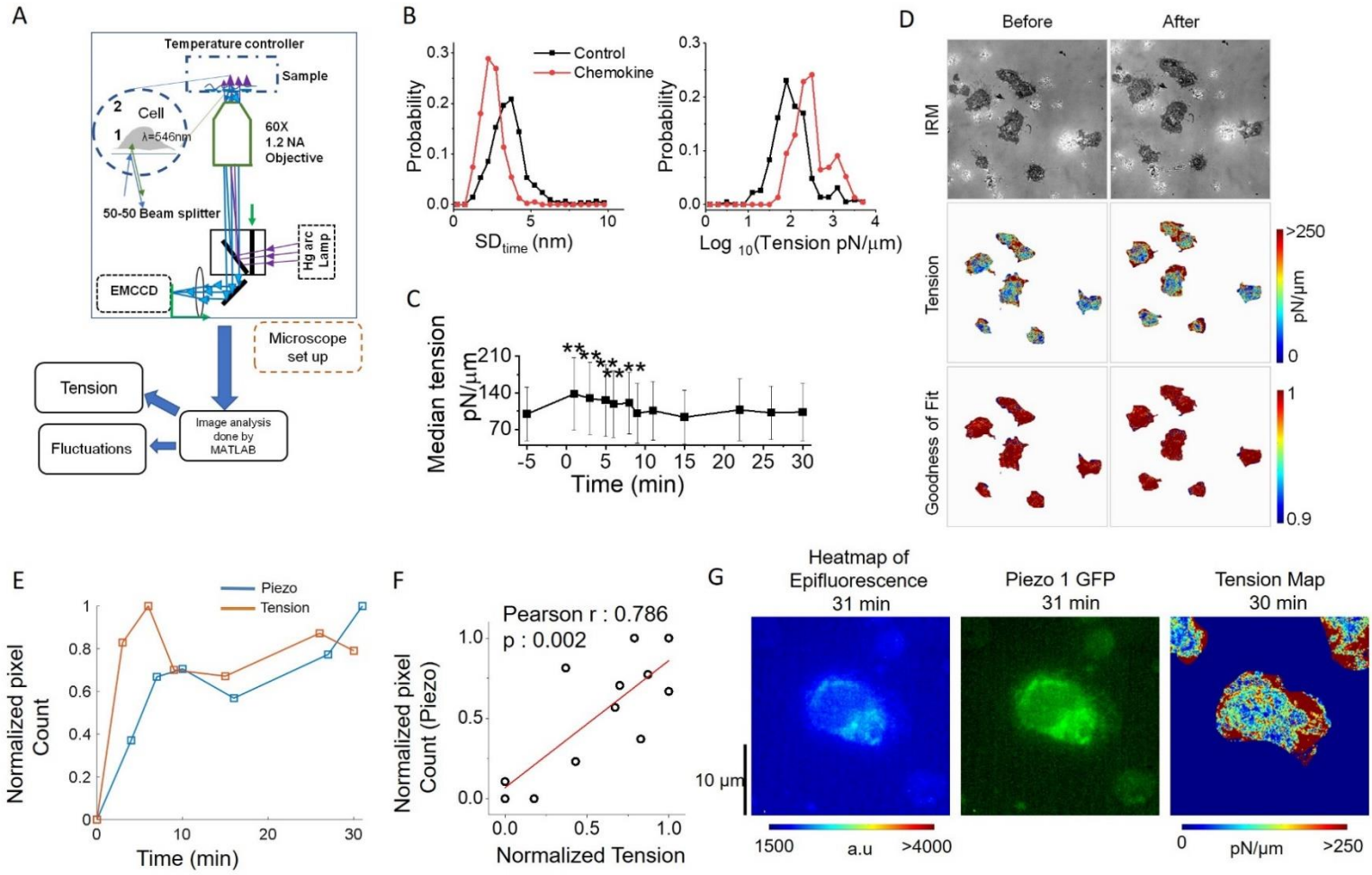

Figure 2

Figure 2. Piezo1 redistribution in migrating T cells follow increased membrane tension in the leading edge

A. Schematic illustration of interference reflection microscopy imaging setup. **B.** Probability distribution of amplitude of temporal fluctuations (SD_{time}, left) and tension (right) before and after addition of chemokines. **C.** Temporal trajectory of tension of cells before and after addition of chemokine with ** indicating significant difference from control. **D.** Representative IRM images of Jurkat cells (top), corresponding tension maps (middle) and R^2 maps (bottom), before and after 3 minutes of chemokine treatment. **E** Correlation between normalized Piezo intensity, tension magnitudes with time. **F.** Scatter plot to show correlation between normalized pixel count of Piezo1 and normalized tension. Piezo1 intensity at specific time-points were correlated with tension magnitudes at the preceding timepoints. Normalization has been done such that the maximum value is set to 1 and others are accordingly scaled. **G.** Colour-coded Piezo1-GFP intensity map (left), epifluorescence image (middle), and tension map (right) of representative Piezo1-GFP expressing Jurkat cell, after 30 minutes of 0.1μg/ml of SDF1α treatment.

693

694

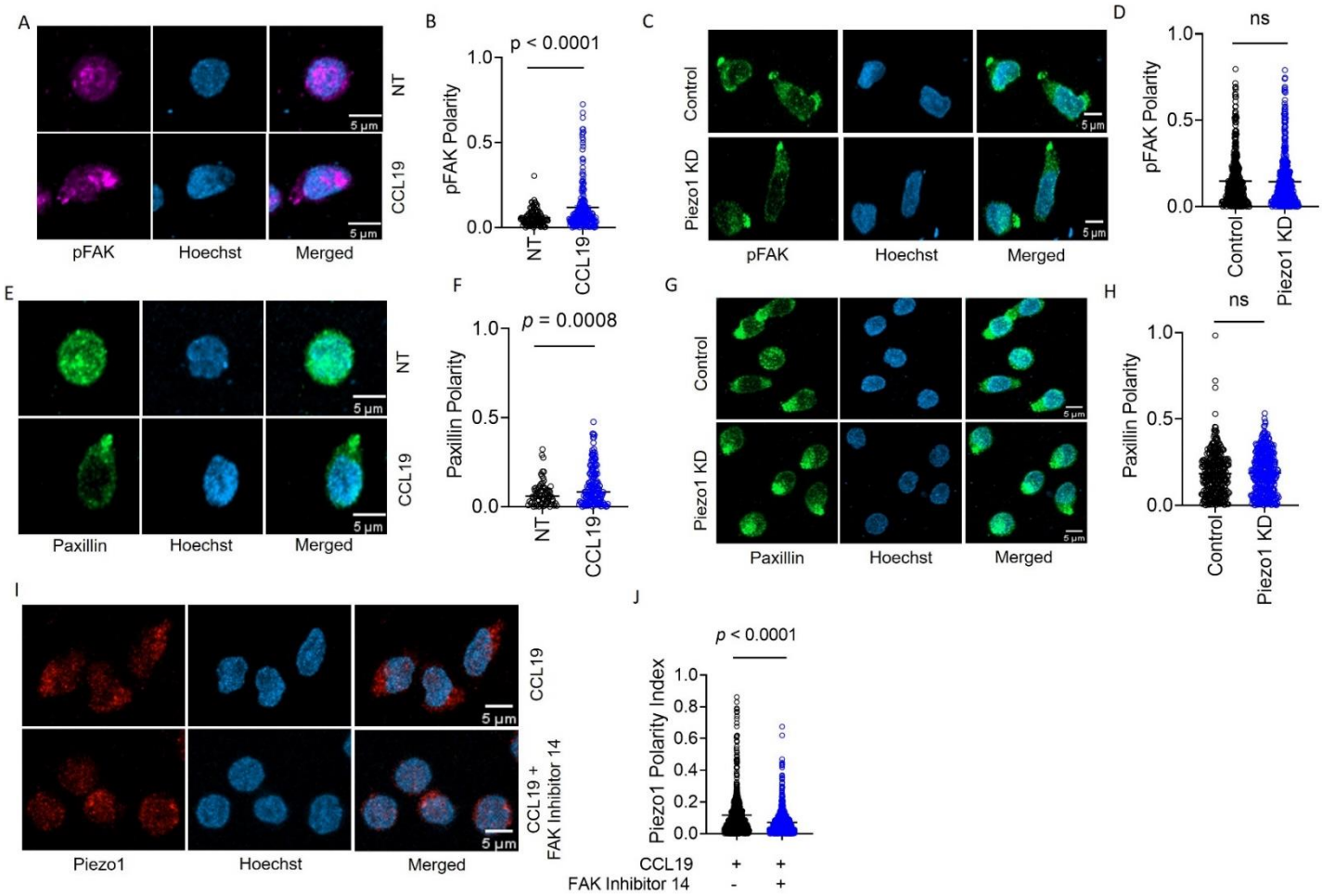

Figure 3

695

696 **Figure 3. Focal adhesion following chemokine receptor activation does not depend on Piezo1**

697 **A.** Representative confocal images of human CD4⁺ T lymphocytes, fixed and stained for phospho-FAK
698 (pFAK) under untreated and CCL19-treated conditions. **B.** Increased polarity of pFAK upon chemokine
699 stimulation of CD4⁺ T lymphocytes as compared to unstimulated controls. N > 120 cells, each. **C.**
700 Representative confocal images of pFAK distribution in control and Piezo1 siRNA-transfected CD4⁺ T
701 lymphocytes stimulated with chemokine. **D**. Comparison of pFAK polarity in CCL19-stimulated control
702 and Piezo1-knockdown CD4⁺ T lymphocytes. n > 450 random cells, each. **E.** Representative confocal
703 images of paxillin distribution in untreated versus CCL19-stimulated CD4⁺ T lymphocytes. **F.** Increased
704 paxillin polarity in response to CCL19 stimulation as compared to untreated CD4⁺ T lymphocytes.
705 Untreated n > 70, CCL19-treated n > 150. **G.** Representative confocal images of immunostained paxillin
706 in chemokine-stimulated, control and Piezo1-knockdown CD4⁺ T lymphocytes. **H**. Comparison of
707 paxillin polarity in CCL19-stimulated control and Piezo1-knockdown CD4⁺ T lymphocytes. n > 550
708 random cells, each. **I.** Representative confocal images of stained Piezo1 in CD4⁺ T cells stimulated with

709 CCL19 in the presence or absence of FAK inhibitor 14. **J.** Effect of FAK inhibition on Piezo1 polarity in
710 $CD4^+$ T lymphocytes stimulated with recombinant CCL19 versus untreated cells. n > 600 random cells,
711 each. Data represented from at least 3 independent experiments.

712

713

714

715

716

717

718

719

720

721

722

723

724

725

726

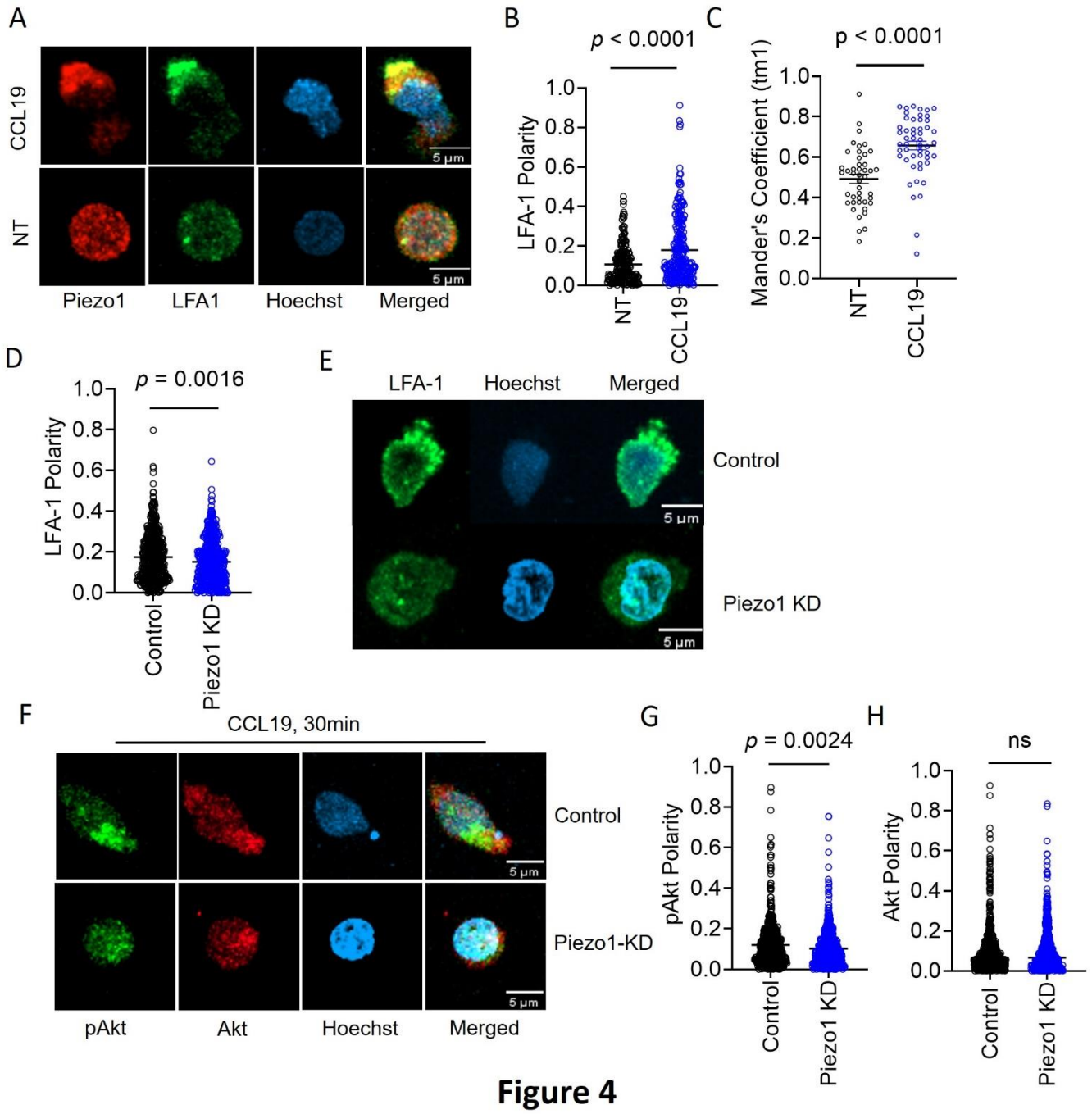

Figure 4

Figure 4. Membrane recruitment of LFA1 on chemokine receptor activation disrupts with Piezo1 deficiency.

A. Representative confocal images of fixed, immunostained Piezo1 and LFA1 in unstimulated and CCL19-stimulated CD4$^+$ T lymphocytes. **B.** Increased LFA1 polarity in response to recombinant CCL19 stimulation in CD4$^+$ T cells. n > 295 random cells, each. **C.** Manders' co-localisation analysis of Piezo1 and LFA1 in untreated and CCL19-treated CD4$^+$ T lymphocytes. **D.** Comparison of LFA1 polarity in chemokine-treated control and Piezo1 knockdown CD4$^+$ T lymphocytes. **E.** Representative confocal stained images of LFA1 polarity of CCL19-treated control and Piezo1-knockdown CD4$^+$ T lymphocytes. n > 490 random cells, each. **F.** Representative confocal images of phospho-Akt (pAkt) and Akt

736 distribution upon chemokine treatment of control and Piezo1-knockdown cells. **G & H.** Quantitative
737 analyses of pAkt (M) and Akt (N) polarity in control and Piezo1-knockdown cells after CCL19-
738 treatment. n > 580 random cells, each. Data represented from at least 3 independent experiments.

739

740

741

742

743

744

745

746

747

748

749

750

751

752

753

754

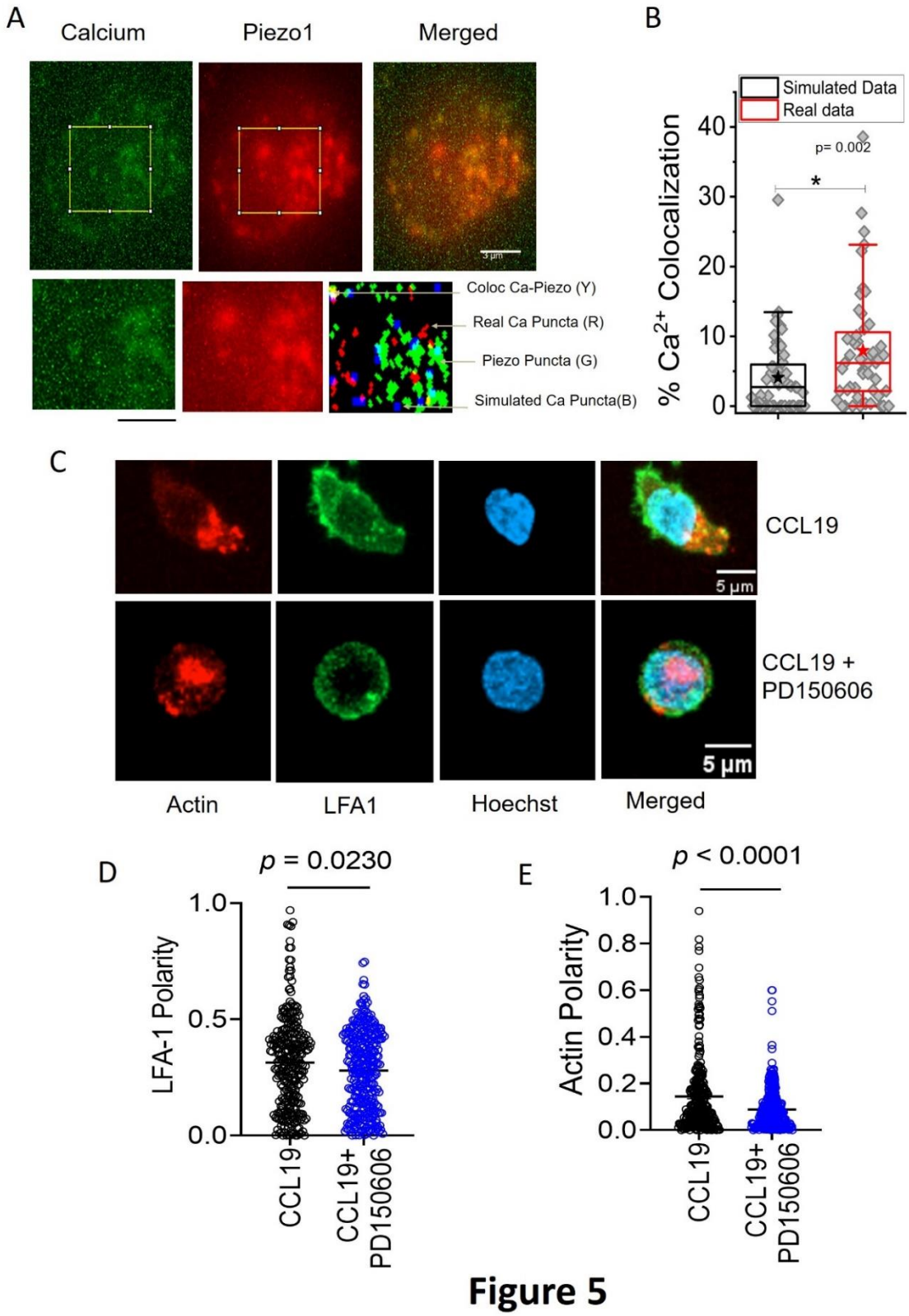

Figure 5. Local Ca^{2+} mobilization with Piezo1 redistribution upon chemokine stimulation.

A. Representative TIRF image of a Jurkat Cell stained with Fluo3AM and transiently expressing with Piezo1 mCherry. Lower panel: zoomed in image and overlap of binary images of objects detected from

758 Calcium and Piezo channels as well as simulated randomly placed punctas having similar total (in the
759 zoomed in section) and average area as that of the Calcium punctas detected in the real images.
760 Overlap RGB image shows the overlap between Real Calcium (Red) and piezo puncta (Green), overlap
761 puncta (Yellow), simulated calcium puncta (blue). **B.** Comparison between percentage calcium
762 colocalization of simulated data and real data. * Denote p value < 0.05 calculated using Mann Whitney
763 U test. N cell= 52 (13 cells x 4 time points). NROIS= 52. **C.** Representative confocal images of LFA1 and
764 actin distribution in CCL19-stimulated CD4+ T lymphocytes with or without inhibition of calpain.
765 100µM of PD15606 was added to the cells 1 hour prior to addition of chemokine. Quantitative
766 comparisons of **D.** LFA1 and **E.** actin polarity upon chemokine stimulation, in the presence or absence
767 of calpain pre-inhibition. N > 290 random cells, each. Data represented is of at least 3 independent
768 experiments.

769

770

771

772

773

774

775

776

777

778

779

780

781

782

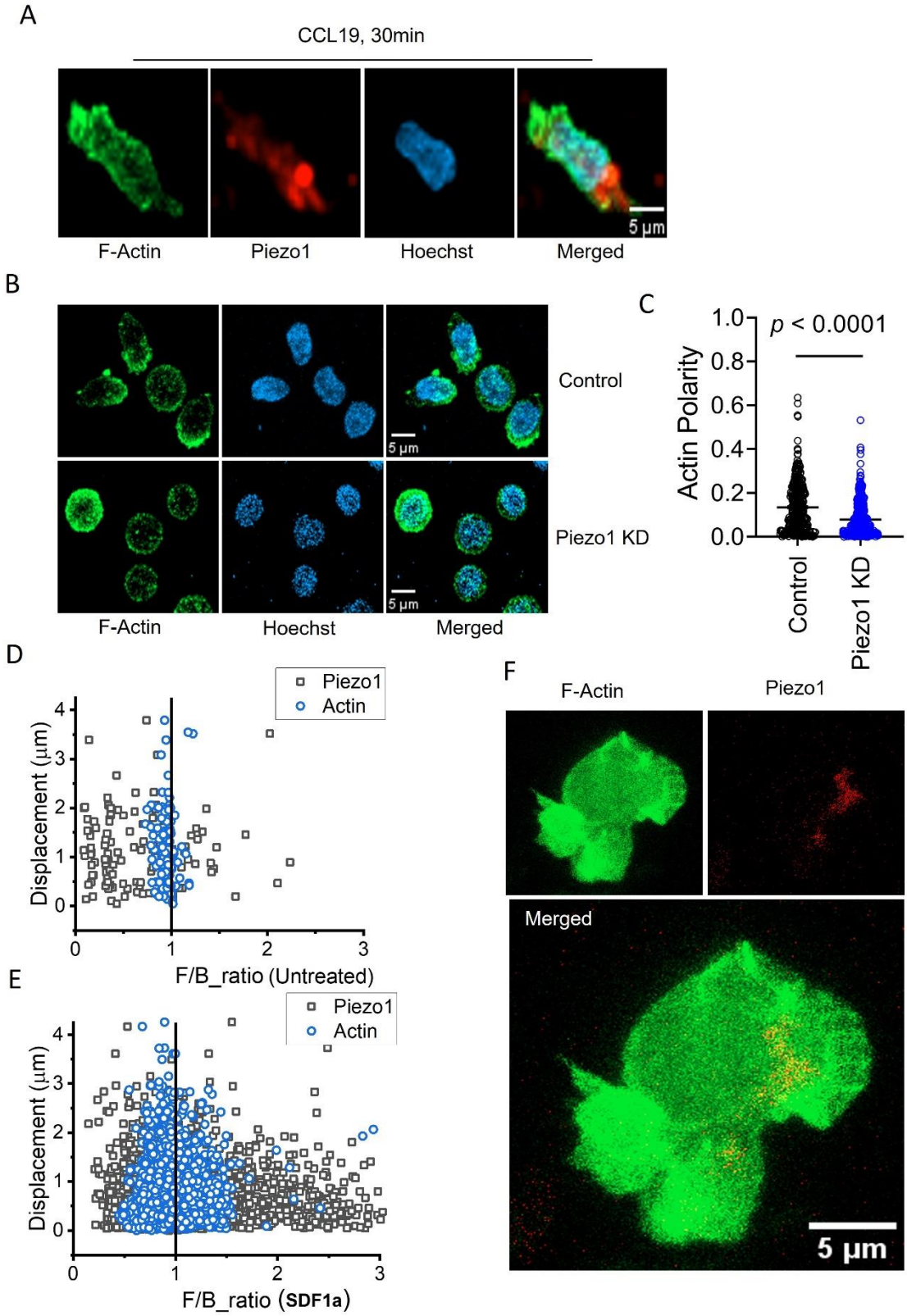

Figure 6

783 **Figure 6. Piezo1 deficiency disrupts F-actin retrograde flow in T cells despite chemokine receptor**
784 **activation.**

785 **A.** Representative fixed confocal images of actin and Piezo1 distribution in $CD4^+$ T lymphocytes after
786 30 mins of 0.5µg/ml recombinant CCL19 treatment. **B.** Quantitative comparison of actin polarity in
787 control and Piezo1-knockdown $CD4^+$ T lymphocytes cells after 30 mins of chemokine treatment. n >
788 300 random cells, each. **C.** Representative fixed confocal images of actin distribution in chemokine-
789 treated, control and Piezo1-knockdown $CD4^+$ T lymphocytes. Front-back (F/B) of Piezo1 and actin-GFP
790 in SDF1α treated **(D)** and untreated **(E)** Jurkat cells co-expressing actin-GFP and Piezo1-mCherry. **F.** A
791 snapshot of time-lapse imaging of Piezo1-mCherry and actin-GFP expressing Jurkat cell treated with
792 0.1µg/ml of SDF1α. Image is maximum Z-projection of the cell at 63X/1.40 magnification. Data
793 represented is of at least 3 independent experiments.

794

795

796

797

798

799

800

801

802

803

804

805

806

807

808

809

810

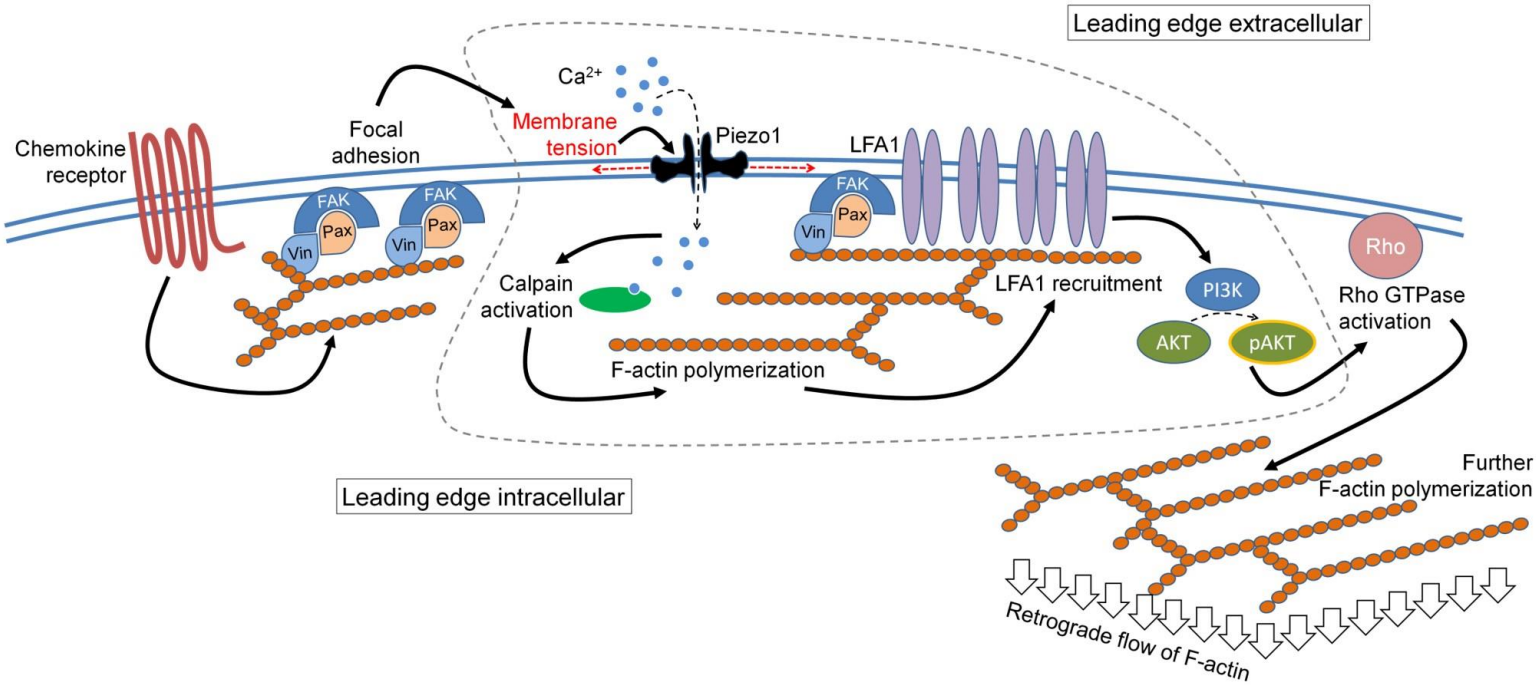

Figure 7

The mechanistic model depicting involvement of Piezo1 mechanosensing in leading edge events in a migrating T cell.

Proposed model suggests chemokine receptor activation in human T cells lead to focal adhesion kinase activation and focal adhesion formation. Focal adhesions lead to localized increase in membrane tension at the leading edge plasma membrane which leads to Piezo1 recruitment and activation. Piezo1 activation leads to calpain activation which potentially drives further cytoskeletal consolidation to recruit integrin LFA1. LFA1 recruitment and activation lead to phosphorylation of AKT and downstream signaling eventually driving the retrograde actin flow in migrating human T cells.

823 **FIGURE LEGENDS**

824 **Figure 1. Piezo1 deficiency abrogates integrin-dependent motility in human T cells which is**
825 **mediated through redistribution of Piezo1 at the leading edge in response to chemokine**
826 **stimulation.**

827 **A.** MSD versus time calculated for GFP^+ (potential Piezo1-knockdown cells) and GFP^- (potential control
828 cells) in GFP plasmid and Piezo1 siRNA co-transfected human $CD4^+$ T lymphocytes, that were allowed
829 to migrate in presence of recombinant CCL19 on ICAM1-coated dishes.**B.** Representative tracks of
830 GFP^+ and GFP^- $CD4^+$ T lymphocytes. Comparisons of **C.** % GFP^+ cells after 72 hours of nucleofection **D**
831 **& E.** 3D transwell migration assay of siRNA-transfected primary human $CD4^+$ T lymphocytes (D) and
832 Jurkat T cells (E), respectively. Data representative of at least 3 independent experiments. **F.**
833 Representative confocal images of Piezo1 distribution in fixed untreated and CCL19-treated $CD4^+$ T
834 lymphocytes. 63X oil magnification. **G.** Comparison between Piezo1 polarity index calculated for fixed,
835 stained, human $CD4^+$ T lymphocytes with or without 0.5µg/ml CCL19 treatment for 20-30 minutes. n
836 > 510 random cells, each. **H.** Piezo1 polarity index calculated for Jurkat cells, expressing mCherry-
837 tagged Piezo1 during live-cell tracking in the presence of recombinant SDF1α. Each dot represents
838 polarity index of each cell, averaged over all the time-frames. **I.** Representative time kinetics of particle
839 image velocimetry (PIV) analysis of Piezo1-mcherry transfected Jurkat cells, allowed to move on ICAM-
840 coated dishes in the presence of recombinant SDF1α. Top panel: No chemokine. Bottom Panel: SDF1α.
841 All data is representative of at least 3 independent experiments.

842

843 **Figure 2. Piezo1 redistribution in migrating T cells follow increased membrane tension in the leading**
844 **edge**

845 **A.** Schematic illustration of interference reflection microscopy imaging setup. **B.** Probability
846 distribution of amplitude of temporal fluctuations (SD_{time}, left) and tension (right) before and after
847 addition of chemokines. **C.** Temporal trajectory of tension of cells before and after addition of
848 chemokine with ** indicating significant difference from control. **D.** Representative IRM images of
849 Jurkat cells (top), corresponding tension maps (middle) and R^2 maps (bottom), before and after 3
850 minutes of chemokine treatment. **E** Correlation between normalized Piezo intensity, tension
851 magnitudes with time. **F.** Scatter plot to show correlation between normalized pixel count of Piezo1
852 and normalized tension. Piezo1 intensity at specific time-points were correlated with tension
853 magnitudes at the preceding timepoints. Normalization has been done such that the maximum value
854 is set to 1 and others are accordingly scaled. **G.** Colour-coded Piezo1-GFP intensity map (left),

855 epifluorescence image (middle), and tension map (right) of representative Piezo1-GFP expressing
856 Jurkat cell, after 30 minutes of 0.1μg/ml of SDF1α treatment.

857

858 **Figure 3. Focal adhesion following chemokine receptor activation does not depend on Piezo1**

859 **A.** Representative confocal images of human $CD4^+$ T lymphocytes, fixed and stained for phospho-FAK
860 (pFAK) under untreated and CCL19-treated conditions. **B.** Increased polarity of pFAK upon chemokine
861 stimulation of $CD4^+$ T lymphocytes as compared to unstimulated controls. N > 120 cells, each. **C.**
862 Representative confocal images of pFAK distribution in control and Piezo1 siRNA-transfected $CD4^+$ T
863 lymphocytes stimulated with chemokine. **D**. Comparison of pFAK polarity in CCL19-stimulated control
864 and Piezo1-knockdown $CD4^+$ T lymphocytes. n > 450 random cells, each. **E.** Representative confocal
865 images of paxillin distribution in untreated versus CCL19-stimulated $CD4^+$ T lymphocytes. **F.** Increased
866 paxillin polarity in response to CCL19 stimulation as compared to untreated $CD4^+$ T lymphocytes.
867 Untreated n > 70, CCL19-treated n > 150. **G.** Representative confocal images of immunostained paxillin
868 in chemokine-stimulated, control and Piezo1-knockdown $CD4^+$ T lymphocytes. **H**. Comparison of
869 paxillin polarity in CCL19-stimulated control and Piezo1-knockdown $CD4^+$ T lymphocytes. n > 550
870 random cells, each. **I.** Representative confocal images of stained Piezo1 in $CD4^+$ T cells stimulated with
871 CCL19 in the presence or absence of FAK inhibitor 14. **J.** Effect of FAK inhibition on Piezo1 polarity in
872 $CD4^+$ T lymphocytes stimulated with recombinant CCL19 versus untreated cells. n > 600 random cells,
873 each. All data represented is from at least 3 independent experiments.

874

875 **Figure 4. Membrane recruitment of LFA1 on chemokine receptor activation disrupts with Piezo1**
876 **deficiency.**

877 **A.** Representative confocal images of fixed, immunostained Piezo1 and LFA1 in unstimulated and
878 CCL19-stimulated $CD4^+$ T lymphocytes. **B.** Increased LFA1 polarity in response to recombinant CCL19
879 stimulation in $CD4^+$ T cells. n > 295 random cells, each. **C.** Manders' co-localisation analysis of Piezo1
880 and LFA1 in untreated and CCL19-treated $CD4^+$ T lymphocytes. **D.** Comparison of LFA1 polarity in
881 chemokine-treated control and Piezo1 knockdown $CD4^+$ T lymphocytes. n > 490 random cells, each.
882 **E.** Representative confocal stained images of LFA1 polarity of CCL19-treated control and Piezo1-
883 knockdown $CD4^+$ T lymphocytes. **F.** Representative confocal images of phospho-Akt (pAkt) and Akt
884 distribution upon chemokine treatment of control and Piezo1-knockdown cells. **G & H.** Quantitative
885 analyses of pAkt (M) and Akt (N) polarity in control and Piezo1-knockdown cells after CCL19-

886 treatment. n > 580 random cells, each. All data is representative of at least 3 independent
887 experiments.

888

889 **Figure 5. Local Ca^{2+} mobilization with Piezo1 redistribution upon chemokine stimulation.**

890 **A.** Representative TIRF image of a Jurkat Cell stained with Fluo3AM and transiently expressing with
891 Piezo1 mCherry. Lower panel: zoomed in image and overlap of binary images of objects detected from
892 Calcium and Piezo channels as well as simulated randomly placed punctas having similar total (in the
893 zoomed in section) and average area as that of the Calcium punctas detected in the real images.
894 Overlap RGB image shows the overlap between Real Calcium (Red) and piezo puncta (Green), overlap
895 puncta (Yellow), simulated calcium puncta (blue). **B.** Comparison between percentage calcium
896 colocalization of simulated data and real data. * Denote p value < 0.05 calculated using Mann Whitney
897 U test. N cell= 52 (13 cells x 4 time points). NROIS= 52. **C.** Representative confocal images of LFA1 and
898 actin distribution in CCL19-stimulated CD4+ T lymphocytes with or without inhibition of calpain.
899 100µM of PD15606 was added to the cells 1 hour prior to addition of chemokine. Quantitative
900 comparisons of **D.** LFA1 and **E.** actin polarity upon chemokine stimulation, in the presence or absence
901 of calpain pre-inhibition. N > 290 random cells, each. All data is generated from at least 3 independent
902 experiments.

903

904 **Figure 6. Piezo1 deficiency disrupts F-actin retrograde flow in T cells despite chemokine receptor**
905 **activation.**

906 **A.** Representative fixed confocal images of actin and Piezo1 distribution in $CD4^+$ T lymphocytes after
907 30 mins of 0.5µg/ml recombinant CCL19 treatment. **B.** Representative fixed confocal images of actin
908 distribution in chemokine-treated, control and Piezo1-knockdown CD4+ T lymphocytes. **C.**
909 Quantitative comparison of actin polarity in control and Piezo1-knockdown $CD4^+$ T lymphocytes cells
910 after 30 mins of chemokine treatment. n > 300 random cells, each. Front-back (F/B) of Piezo1 and
911 actin-GFP in SDF1α treated **(D)** and untreated **(E)** Jurkat cells co-expressing actin-GFP and Piezo1-
912 mCherry. **F.** A snapshot of time-lapse imaging of Piezo1-mCherry and actin-GFP expressing Jurkat cell
913 treated with 0.1µg/ml of SDF1α. Image is maximum Z-projection of the cell at 63X/1.40 magnification.
914 All data is generated from at least 3 independent experiments.

915

916

917 **Figure 7. The mechanistic model depicting involvement of Piezo1 mechanosensing in leading edge**
918 **events in a migrating T cell.**

919 Proposed model suggests chemokine receptor activation in human T cells lead to focal adhesion kinase
920 activation and focal adhesion formation. Focal adhesions lead to localized increase in membrane
921 tension at the leading edge plasma membrane which leads to Piezo1 recruitment and activation.
922 Piezo1 activation leads to calpain activation which potentially drives further cytoskeletal consolidation
923 to recruit integrin LFA1. LFA1 recruitment and activation lead to phosphorylation of AKT and
924 downstream signaling eventually driving the retrograde actin flow in migrating human T cells.

925

926 **FIGURE SUPPLEMENTS LEGENDS**

927 **Figure 1-figure supplement 1**. **A.** Quantitative PCR analysis of Piezo1 and Piezo2 relative expression,
928 in control and Piezo1 siRNA-transfected $CD4^+$ T lymphocytes. **B.** Flow cytometric measurement of
929 Piezo1 mean fluorescence intensity, MFI (left: surface staining; right: intracellular staining) in Piezo1
930 siRNA and GFP co-transfected cells. **C.** Representative histograms (right two panels) of Piezo1 MFI in
931 GFP (-) and GFP (+) cells in surface stained (left) and intracellularly stained (right) cells. **D.**
932 Representative immunofluorescence image 2D tracks (left), GFP signal (middle) and cell trace violet
933 signal of all cells (right). 20X magnification. E. MSD tracks of control siRNA (n = 357 cells) and Piezo1
934 siRNA-transfected $CD4^+$ T cells (n = 348 cells) on ICAM1-coated wells in the presence of CCL19. **F.** Effect
935 of Piezo1 inhibition by GsMTx4 on 3D ICAM1-coated transwell migration. **G**. Representative confocal
936 images depicting anti-polarity of Piezo1 and CD44 (uropod) in untreated and CCL19-stimulated
937 conditions. **H**. Polarity indices calculated for Piezo1 and CD44, where negative polarity for Piezo1
938 means anti-polarity (described in detailed in Methods section). N = 69 cells, each. All data shown is
939 representative of at least 3 independent experiments.

940

941 **Figure 2-figure supplement 1. A.** Probability distribution of temporal fluctuation (left) and tension
942 (right) followed over time, **B.** Tension maps showing high-tension edges aligning with direction of cell
943 migration (arrows) before and after addition of chemokine. Cells from 2 fields (top and bottom panel)
944 are depicted in the figure. **C.** Box plots of time-kinetics of tension (upper left), confinement (upper
945 right), effective cytoplasmic viscosity (lower left)**. D.** Temporal trajectory of effective cytoplasmic
946 viscosity (left) and confinement (right) of cells before and after addition of chemokine with **
947 indicating significant difference from control. ns = p>0.0042, *p<0.0042, **p<0.000083 derived using
948 Mann-Whitney U Test with Bonferroni correction. N_{cells} =21, $N_{FBR\ (control)}$ = 1594, $N_{FBR\ (1\ min)}$ =1228, $N_{FBR\ (3}$

949 min) =643, $N_{FBR\ (5\ min)}$ = 1349, $N_{FBR\ (6\ min)}$ =594, $N_{FBR\ (8\ min)}$ =1056, $N_{FBR\ (9\ min)}$ =1562, $N_{FBR\ (11\ min)}$ =638, $N_{FBR\ (15\ min)}$
950 =1843, $N_{FBR\ (22\ min)}$ =741, $N_{FBR\ (26\ min)}$ =2019, $N_{FBR\ (30\ min)}$ =2746. Scale bar = 10 µm.

951

952 **Figure 3-figure supplement 1. A.** Mean signal intensity of pFAK in CCL19-treated control and Piezo1
953 KD cells (n > 440 random cells, each). **B.** Mean signal intensity of paxillin in CCL19-treated control and
954 Piezo1 KD cells (n > 780 random cells, each). **C.** Representative images of pFAK and Piezo1
955 colocalization in untreated (top panel) and CCL19-treated (bottom panel) $CD4^+$ T cells.

956

957 **Figure 5- figure supplement 1. A.** Scatter plot of how percentage area of Ca^{2+} peaks (real and
958 simulated) that overlap with Piezo1 varies with area fraction of Piezo1 showing comparison between
959 real and simulated data. **B.** Color matrix of p-value of comparison of % overlap obtained using real
960 data and simulated data. Color denotes p-value. As 'x' increases maximum object size used for Piezo1
961 signal changes. As 'y' increases maximum object size used for Ca^{2+} signal changes. **C.** Representative
962 confocal images of human $CD4^+$ T cells fixed and stained for phosphorylated FAK. Cells were treated
963 with CCL19 with or without prior incubation with calpain inhibitor-PD150606. **D.** Comparison of pFAK
964 polarity of cells stimulated with CCL19, with or without prior calpain inhibition. n > 230 random cells,
965 each.

966

967 **Figure 6-figure supplement 1. A.** Representative 2D confocal image of Jurkat cell expressing Piezo1
968 mCherry and actin GFP in the absence (top panel) or presence (bottom panel) of recombinant SDF1α.
969 **B.** Box plots depicting Piezo1 mCherry (left) and actin-GFP (right) front-back polarity in untreated (NT)
970 and chemokine-stimulated conditions. **C.** Polar plots depicting relative Piezo1 mCherry and actin-GFP
971 spatial distribution in Jurkat cells with respect to direction of cell trajectory in untreated (top panel)
972 and SDF1α (bottom panel) treated cells. Spatial distribution was calculated for all the time points of
973 time-lapse imaging (see methods).

974

975 **Methods-figure supplement 1.** Representative analyses for calculation of cell polarity of **A.** Piezo1
976 (fixed); **B.** Piezo1 mCherry (live); **C.** phosphorylated FAK (pFAK, fixed cell); **D.** paxillin (fixed cell); **E.**
977 CD11a/LFA1 (fixed cell); **F.** actin (fixed cell). Region-of-interest identifying cell boundary and polarity
978 indices mentioned. All analyses performed on Fiji (see methods).

979

980 **VIDEOS LEGENDS**

981 **Video 1.** Representative video of cell trace-stained $CD4^+$ T lymphocytes transfected with GFP construct
982 and Piezo1 siRNA, in the presence of recombinant human CCL19 on ICAM1-coated plates, for a total
983 duration 15 minutes at 30 seconds per frame. The left panel represents superimposed cell trace and
984 GFP signals of moving cells. The right panel shows tracks of the moving cells. Boxed cells are GFP^+ cells.
985 20X Magnification. Related to Figure 1A-C and Figure 1-figure supplement 1D.

986 **Video 2.** Representative 3D projection of Z-stacks of $CD4^+$ T lymphocyte treated with recombinant
987 human CCL19 for 15 minutes, immunostained with Piezo1 antibody and Hoechst. 63X magnification.
988 Related to Figure 1F.

989 **Video 3.** Representative immunofluorescence time-lapse video of Piezo1-mCherry expressing Jurkat
990 cell moving on ICAM1-coated dish in the presence of recombinant human SDF1α. Images were
991 acquired manually for a total duration of 15 minutes at 1 minute per frame interval. Images were
992 captured at 40X magnification. Related to Figure 1I.

993 **Video 4.** Representative 3D rendering of confocal Z-stacks of $CD4^+$ T lymphocyte treated with
994 recombinant human CCL19 for 10 minutes, immunostained with phosphorylated FAK antibody and
995 Hoechst. 63X magnification. Related to Figure 3A.

996 **Video 5.** Representative 3D rendering of confocal Z-stacks of $CD4^+$ T lymphocyte depicting Piezo1 and
997 CD11a/LFA-1 distribution, upon 30 minutes of recombinant CCL19 treatment. 63X magnification.
998 Related to Figure 4A.

999 **Video 6.** Representative 3D rendering of confocal Z-stacks of control siRNA-transfected $CD4^+$ T
1000 lymphocyte depicting CD11a/LFA-1 polarity, upon 30 minutes of recombinant CCL19 treatment. 63X
1001 magnification. Related to Figure 4E.

1002 **Video 7.** Representative 3D rendering of confocal Z-stacks of Piezo1 siRNA-transfected $CD4^+$ T
1003 lymphocyte depicting CD11a/LFA-1 polarity, upon 30 minutes of recombinant CCL19 treatment. 63X
1004 magnification. Related to Figure 4E.

1005 **Video 8.** Representative 3D rendering of confocal Z-stacks of control siRNA-transfected $CD4^+$ T
1006 lymphocyte depicting phosphorylated Akt polarity, upon 30 minutes of recombinant CCL19 treatment.
1007 63X magnification. Related to Figure 4F.

1008 **Video 9.** Representative 3D rendering of confocal Z-stacks of Piezo1 siRNA-transfected $CD4^+$ T
1009 lymphocyte depicting phosphorylated Akt polarity, upon 30 minutes of recombinant CCL19 treatment.
1010 63X magnification. Related to Figure 4F.

1011 **Video 10.** Representative 3D rendering of confocal Z-stacks of $CD4^+$ T lymphocyte depicting Piezo1
1012 and actin distribution, upon 30 minutes of recombinant CCL19 treatment. 63X magnification. Related
1013 to Figure 6A.

1014 **Video 11.** Representative 3D rendering of confocal Z-stacks of control siRNA-transfected $CD4^+$ T
1015 lymphocyte depicting actin polarity, upon 30 minutes of recombinant CCL19 treatment. 63X
1016 magnification. Related to Fig. 6B.

1017 **Video 12.** Representative 3D rendering of confocal Z-stacks of Piezo1 siRNA-transfected $CD4^+$ T
1018 lymphocyte depicting loss of actin polarity, after 30 minutes of recombinant CCL19 treatment. 63X
1019 magnification. Related to Fig. 6B.

1020 **Video 13.** Representative time-lapse video of Piezo1-mCherry/actin-GFP expressing Jurkat cell,
1021 moving on ICAM1-coated dish in the presence of recombinant human SDF1α. Images were acquired
1022 as a Z-stack (1µm per stack) at 63X/1.40 oil magnification. Total duration of time-lapse was 5 minutes
1023 at 30 seconds per frame. Images are represented as maximum intensity projection of the Z stack.
1024 Related to Figure 6F.

1025

1026 **SUPPLEMENTARY FILES**

1027 **Supplementary File 1.** Supplementary File 1 includes a detailed list of key resources used in the study.

1028 **Supplementary File 2:** Supplementary File 2 is an excel file containing all data corresponding to each
1029 figure mentioned in the study.

1030 **Supplementary File 3:** Supplementary File 3 includes a zip file containing codes used in Fiji (.ijm files)
1031 and MATLAB (.m files) image analysis.

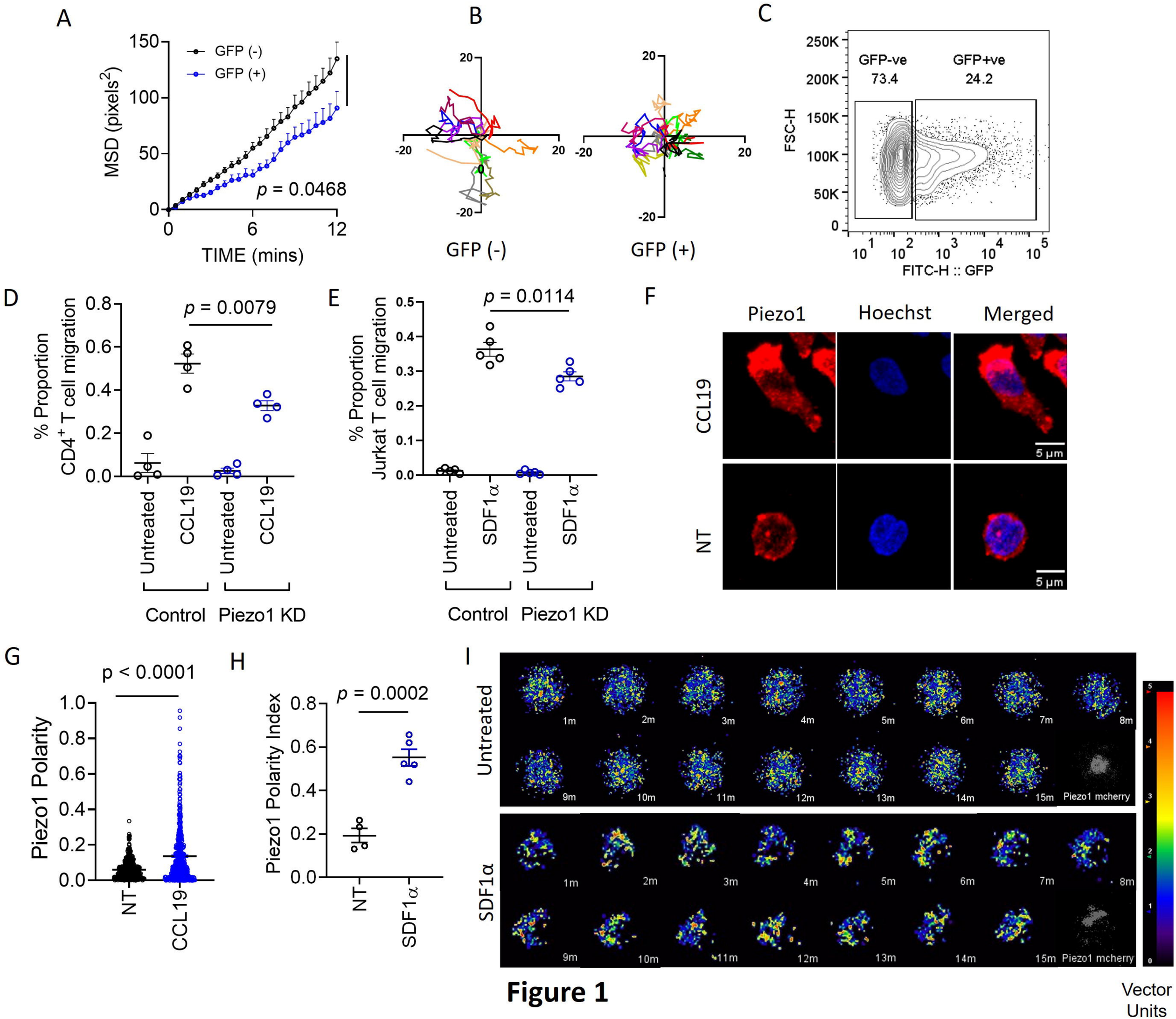
A
MSD (pixels^2)
GFP (-)
GFP (+)
p = 0.0468
TIME (mins)
B
GFP (-)
GFP (+)
C
GFP-ve
73.4
GFP+ve
24.2
FSC-H
FITC-H :: GFP
D
% Proportion CD4$^+$ T cell migration
p = 0.0079
Untreated
CCL19
Control
Piezo1 KD
E
% Proportion Jurkat T cell migration
p = 0.0114
Untreated
SDF1α
Control
Piezo1 KD
F
Piezo1
Hoechst
Merged
CCL19
NT
5 µm
G
Piezo1 Polarity
p < 0.0001
NT
CCL19
H
Piezo1 Polarity Index
p = 0.0002
NT
SDF1α
I
Untreated
SDF1α
1m
2m
3m
4m
5m
6m
7m
8m
9m
10m
11m
12m
13m
14m
15m
Piezo1 mcherry
Vector Units

Figure 1

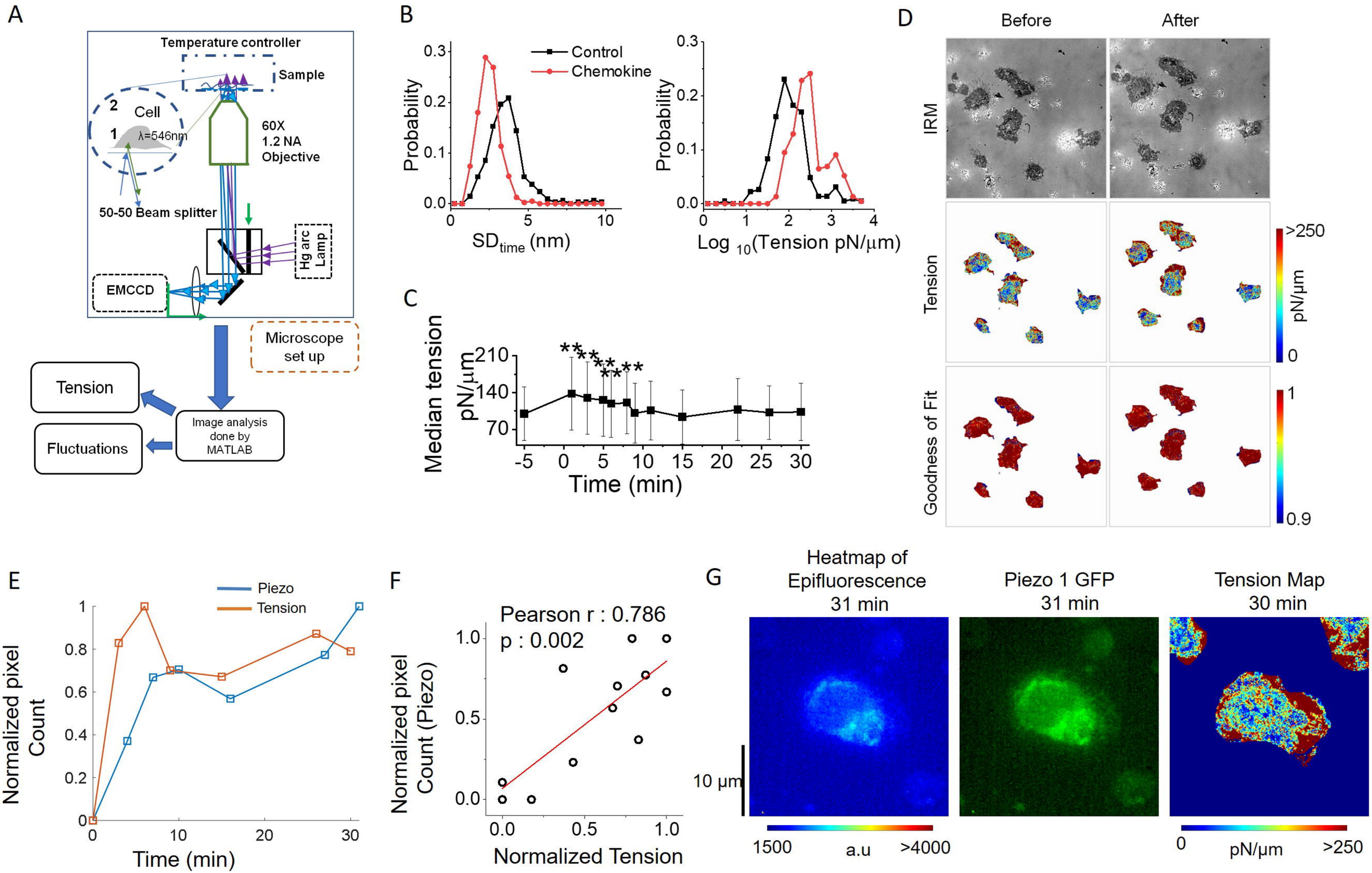
A
Temperature controller
Sample
Cell
2
1
λ=546nm
60X
1.2 NA
Objective
50-50 Beam splitter
Hg arc Lamp
EMCCD
Microscope set up
Tension
Fluctuations
Image analysis done by MATLAB
B
Control
Chemokine
Probability
SD time (nm)
Log 10(Tension pN/μm)
C
Median tension pN/μm
Time (min)
D
Before
After
IRM
Tension
Goodness of Fit
>250
pN/μm
0
1
0.9
E
Piezo
Tension
Normalized pixel Count
Time (min)
F
Pearson r : 0.786
p : 0.002
Normalized pixel Count (Piezo)
Normalized Tension
G
Heatmap of Epifluorescence 31 min
Piezo 1 GFP 31 min
Tension Map 30 min
10 μm
1500
a.u
>4000
0
pN/μm
>250

Figure 2

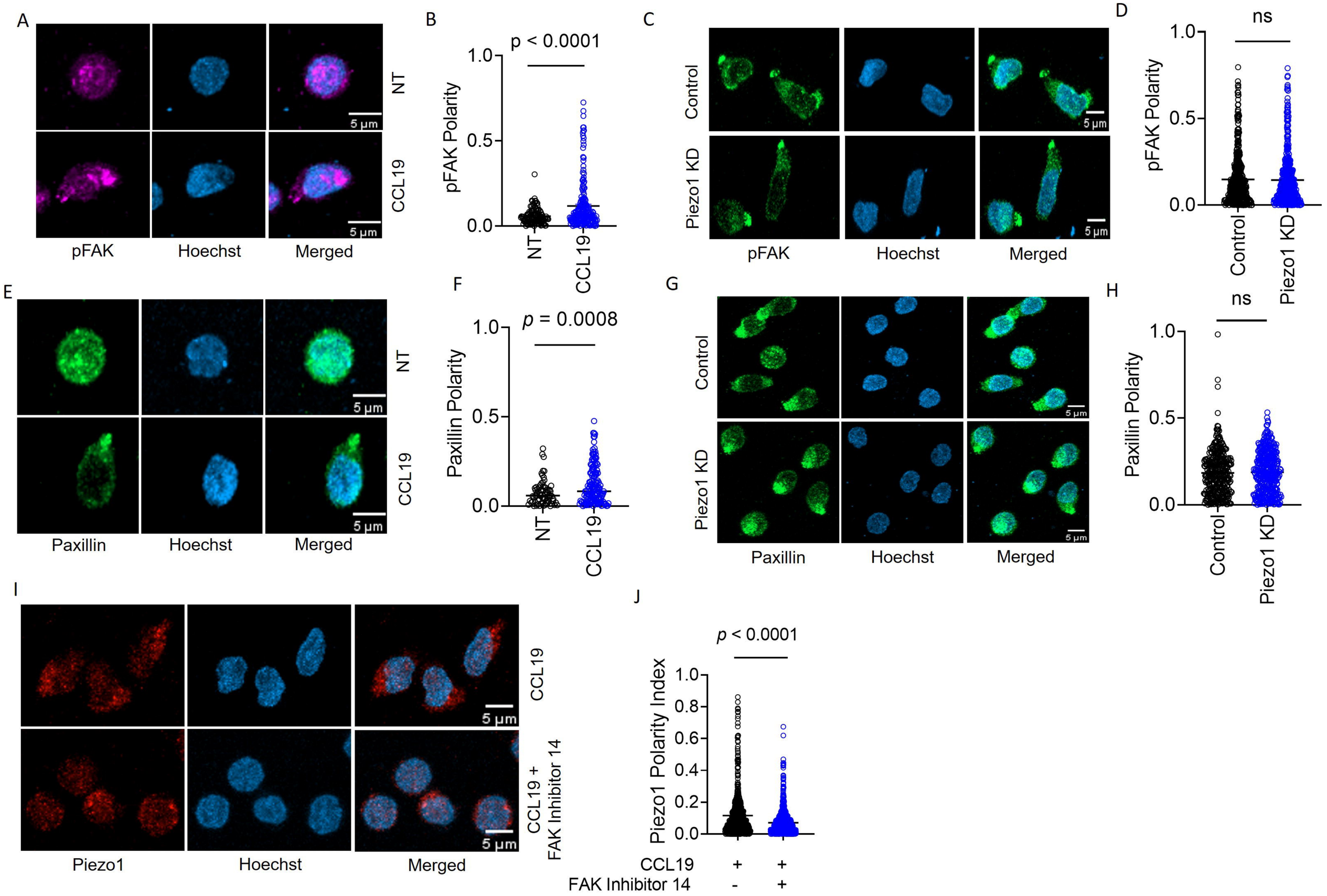
A
NT
CCL19
5 µm
pFAK
Hoechst
Merged
B
p < 0.0001
pFAK Polarity
1.0
0.5
0.0
NT
CCL19
C
Control
Piezo1 KD
5 µm
pFAK
Hoechst
Merged
D
ns
pFAK Polarity
1.0
0.5
0.0
Control
Piezo1 KD
E
NT
CCL19
5 µm
Paxillin
Hoechst
Merged
F
p = 0.0008
Paxillin Polarity
1.0
0.5
0.0
NT
CCL19
G
Control
Piezo1 KD
5 µm
Paxillin
Hoechst
Merged
H
ns
Paxillin Polarity
1.0
0.5
0.0
Control
Piezo1 KD
I
CCL19
CCL19 +
FAK Inhibitor 14
5 µm
Piezo1
Hoechst
Merged
J
p < 0.0001
Piezo1 Polarity Index
1.0
0.8
0.6
0.4
0.2
0.0
CCL19 + +
FAK Inhibitor 14 - +

Figure 3

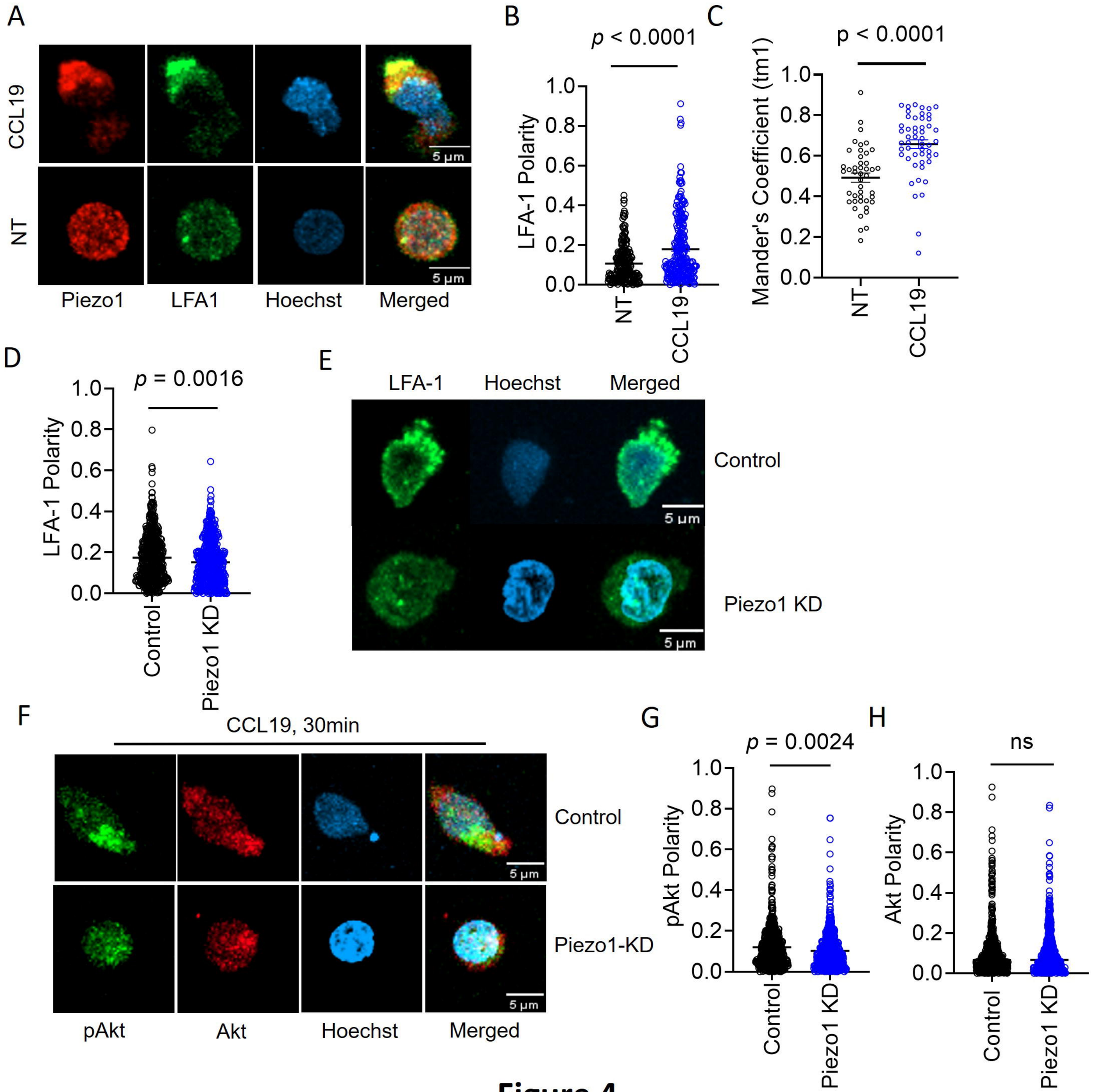
A
CCL19
NT
5 µm
5 µm
Piezo1
LFA1
Hoechst
Merged
B
p < 0.0001
LFA-1 Polarity
1.0
0.8
0.6
0.4
0.2
0.0
NT
CCL19
C
p < 0.0001
Mander's Coefficient (tm1)
1.0
0.8
0.6
0.4
0.2
0.0
NT
CCL19
D
p = 0.0016
LFA-1 Polarity
1.0
0.8
0.6
0.4
0.2
0.0
Control
Piezo1 KD
E
LFA-1
Hoechst
Merged
Control
Piezo1 KD
5 µm
5 µm
F
CCL19, 30min
Control
Piezo1-KD
5 µm
5 µm
pAkt
Akt
Hoechst
Merged
G
p = 0.0024
pAkt Polarity
1.0
0.8
0.6
0.4
0.2
0.0
Control
Piezo1 KD
H
ns
Akt Polarity
1.0
0.8
0.6
0.4
0.2
0.0
Control
Piezo1 KD

Figure 4

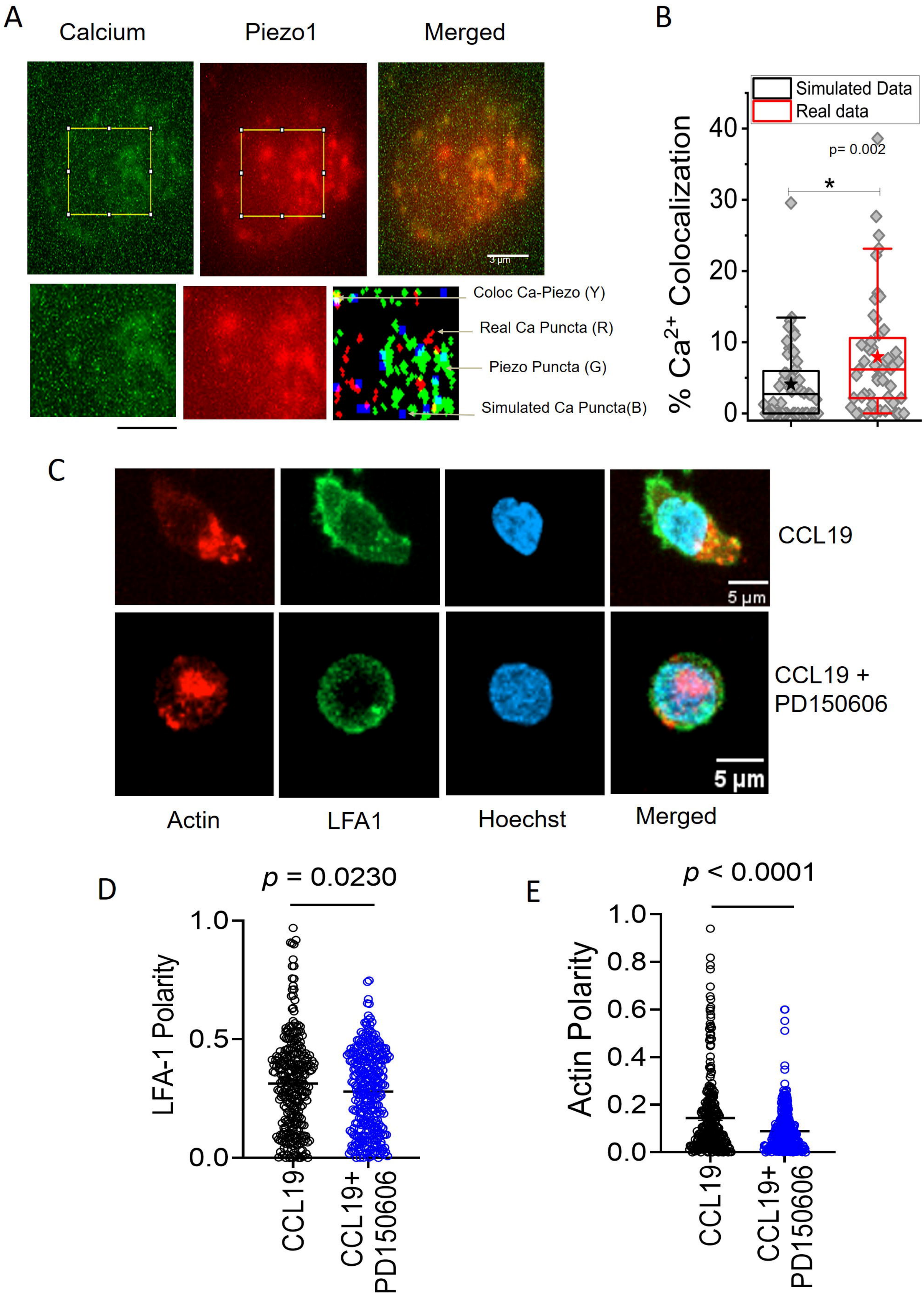
A
Calcium
Piezo1
Merged
3 µm
Coloc Ca-Piezo (Y)
Real Ca Puncta (R)
Piezo Puncta (G)
Simulated Ca Puncta(B)
B
Simulated Data
Real data
p= 0.002
*
% Ca2+ Colocalization
40
30
20
10
0
C
CCL19
5 µm
CCL19 +
PD150606
5 µm
Actin
LFA1
Hoechst
Merged
D
p = 0.0230
LFA-1 Polarity
1.0
0.5
0.0
CCL19
CCL19+
PD150606
E
p < 0.0001
Actin Polarity
1.0
0.8
0.6
0.4
0.2
0.0
CCL19
CCL19+
PD150606

Figure 5

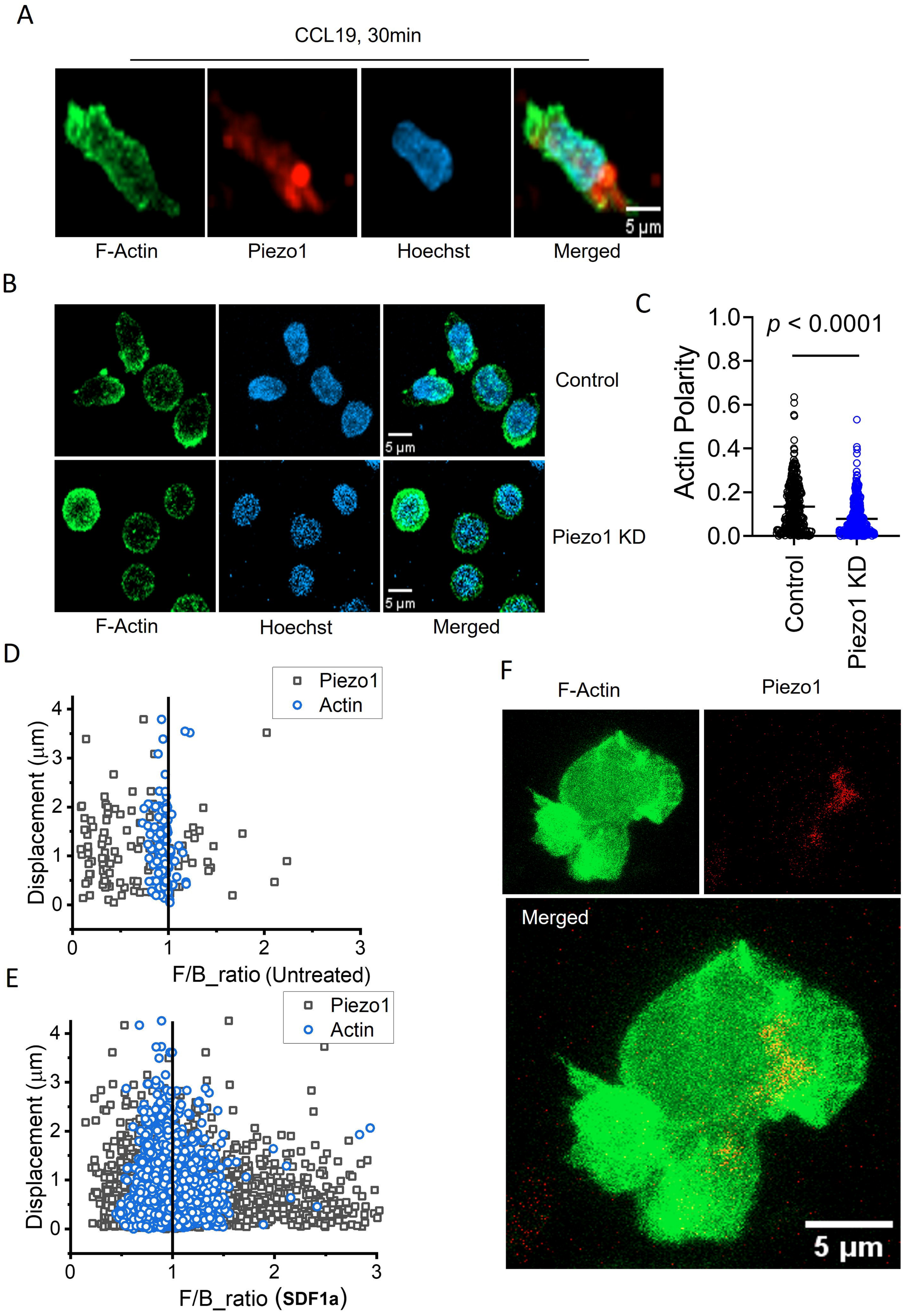
A
CCL19, 30min
F-Actin
Piezo1
Hoechst
Merged
5 µm
B
Control
Piezo1 KD
F-Actin
Hoechst
Merged
5 µm
C
p < 0.0001
Actin Polarity
1.0
0.8
0.6
0.4
0.2
0.0
Control
Piezo1 KD
D
Piezo1
Actin
Displacement (µm)
F/B_ratio (Untreated)
E
Piezo1
Actin
Displacement (µm)
F/B_ratio (SDF1a)
F
F-Actin
Piezo1
Merged
5 µm

Figure 6

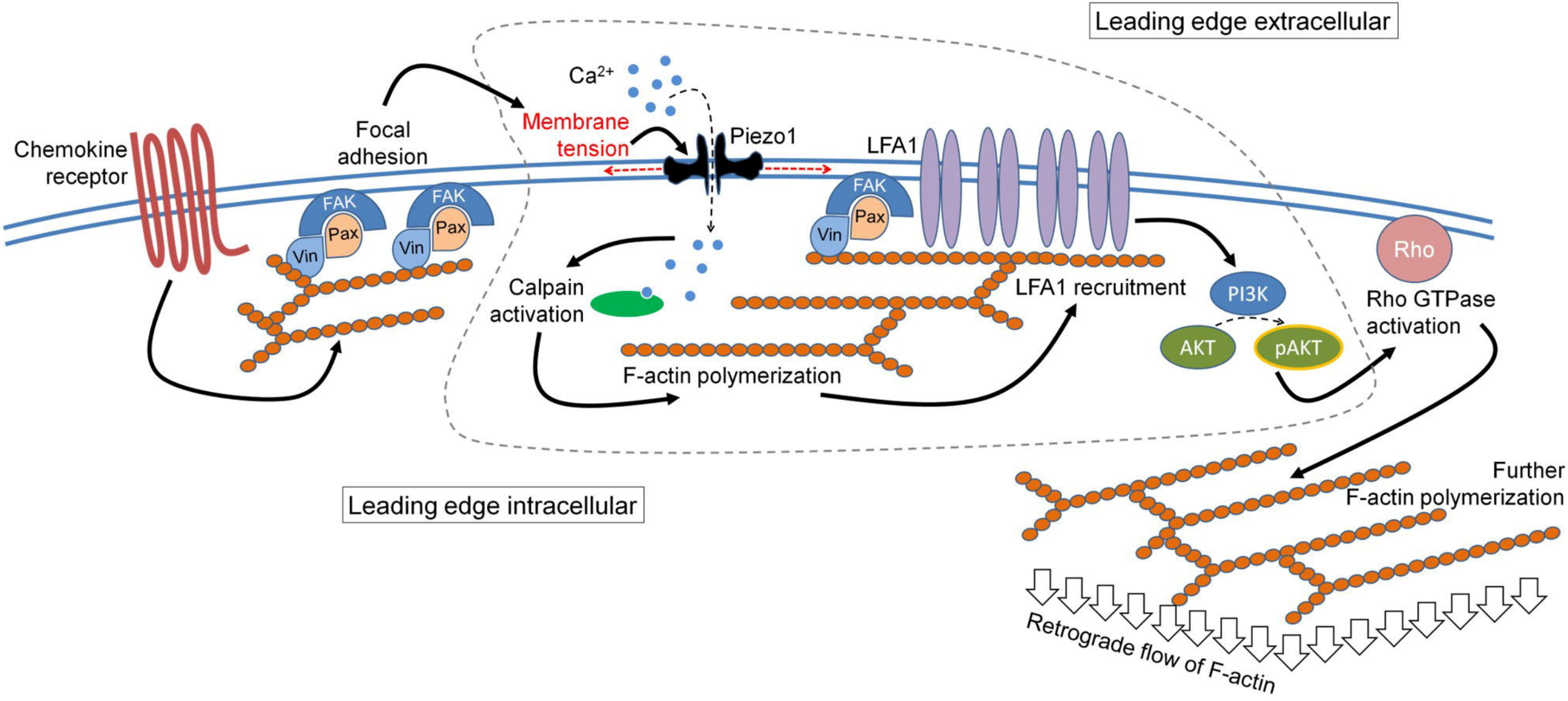
Leading edge extracellular
Ca2+
Chemokine receptor
Focal adhesion
Membrane tension
Piezo1
LFA1
FAK
Pax
Vin
FAK
Pax
Vin
FAK
Pax
Vin
Rho
Calpain activation
LFA1 recruitment
PI3K
Rho GTPase activation
AKT
pAKT
F-actin polymerization
Leading edge intracellular
Further F-actin polymerization
Retrograde flow of F-actin

Figure 7